Rice University

Final Report

U.S. Department of Energy Award Number: DE-FC36-05GO15080

Final Report

Project Title: **Optimization of Nano-Carbon Materials for Hydrogen Sorption**

Partner-participant of	Hydrogen Sorption Center of Excellence
Project Period:	February 1, 2005 to December 31, 2010
Date of Report:	July 26th, 2012
Recipient:	Rice University
Award Number:	DE-FC36-05GO15080
Working Partners:	Rice University
Cost-Sharing Partners:	Rice University
Contacts:	Prof. Boris I. Yakobson, Principal Investigator 713-348-3572, biy@rice.edu Dr. Robert H. Hauge, Co-Principal Investigator 713-348-6384, hauge@rice.edu
DOE Manager:	Jesse Adams

Executive Summary

Research undertaken has added to the understanding of several critical areas, by providing both negative answers (and therefore eliminating expensive further studies of unfeasible paths) and positive feasible options for storage. Theoretical evaluation of the early hypothesis of storage on pure carbon single wall nanotubes (SWNT) has been scrutinized with the use of comprehensive computational methods (and experimental tests by the Center partners), and demonstrated that the fundamentally weak binding energy of hydrogen is not sufficiently enhanced by the SWNT curvature or even defects, which renders carbon nanotubes not practical media. More promising direction taken was towards 3-dimensional architectures of high porosity where concurrent attraction of H_2 molecule to surrounding walls of nano-scale cavities can double or even triple the binding energy and therefore make hydrogen storage feasible even at ambient or somewhat lower temperatures. An efficient computational tool has been developed for the rapid capacity assessment combining (i) carbon-foam structure generation, (ii) accurate empirical force fields, with quantum corrections for the lightweight H_2, and (iii) grand canonical Monte Carlo simulation. This made it possible to suggest optimal designs for carbon nanofoams, obtainable via welding techniques from SWNT or by growth on template-zeolites. As a precursor for 3D-foams, we have investigated experimentally the synthesis of VANTA (Vertically Aligned NanoTube Arrays). This can be used for producing nano-foams. On the other hand, fluorination of VANTA did not show promising increase of hydrogen sorption in several tests and may require further investigation and improvements. Another significant result of this project was in developing a fundamental understanding of the elements of hydrogen spillover mechanisms. The benefit of developed models is the ability to foresee possible directions for further improvement of the spillover mechanism.

***

Project Objectives

- Evaluate theoretically the storage potential of pure carbon nanotubes.
- Identify 3D carbon nanostructures, including those with chemical enhancement groups, for best H-adsorption.
- Maintain production of vertically aligned nanotube arrays (VANTA) for chemical modification to achieve targeted hydrogen adsorption.
- Develop theoretical models for evaluation of hydrogen-3D-Carbon interactions.
- Develop rapid simulation assessment of H_2 physical-sorption capacity, using grand canonical Monte Carlo (GCMC) methods, including quantum corrections.
- Propose comprehensive model of spillover mechanism, including H chemisorption to carbon receptor and functionality of the metal catalyst.

Background / Technical Barriers Addressed

- Efficiently combined simulation methods for H-SWNT and H-"C-foams" interactions.
- Metal-SWNT complexes stability, for better H-adsorption efficiency.
- Densification of VANTA material and its chemical enhancement.
- Determined H-vibration modes for spillover analysis by neutron scattering.
- Modeling of spillover as phase nucleation process.
- Understood and quantified the catalyst function as spillover pump.

Technical Narrative: Tasks Status and Accomplishments

<u>Theoretical evaluation of the storage potential of pure carbon nanotubes</u>
One of the important early tasks of the project was investigation of pure nanotubes as potential storage media. This was based both on experimental evidence derived from preliminary published evidence (by the Center partners and other independent teams, including MIT), and by theoretical analysis at the Air Products Corp. Air Products published data contained intriguing suggestion that the bending-fluctuation curvature of SWNT increases the degree of sp^3 hybridization, and thus promotes H_2 binding. Our early focus on computational studies of the "bare"-SWNT + H_2 and specifically computations of curvature effects served to verify these findings and to determine the feasibility of this path forward.

To this end, over roughly the first two years, we performed an investigation of bistability/bifurcation on the energy surfaces of $C(sp^2)+H_2 \leftrightarrow C(sp^3)+2CH$. Following crude classical-potential simulations (performed with DL_POLY, an acronym from Daresbury Laboratory polymers modeling package) we also focused on analysis of potential wells (as "nano-pumps", using the term of relevant report from NRC Canada, PNAS 2005). Prior to quantum-statistics calculations, we carefully computed the potential surface for H_2 for *different carbon-carrier* geometries. In the

Fig. 1 below, potential surfaces computed are shown, with a hybrid Morse-LJ potential, for an isolated SWNT and for a flattened SWNT of larger diameter, in order to evaluate "tunability" of the pump-effect by the deformations of carbon network. A large-sample configuration that has been evolved with classical molecular dynamics.

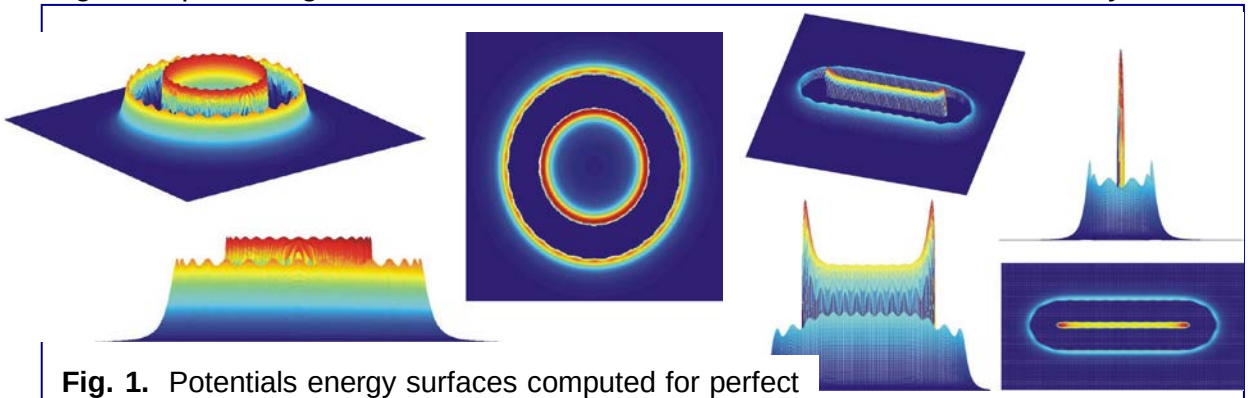

Fig. 1. Potentials energy surfaces computed for perfect (left) and for flattened SWNT of larger diameter (right).

The picture that emerges is that individual C-plane (like flat graphene layer, or curved either tube or large-fullerene wall) provides insufficient attraction for H_2 retention. On the other hand, too tightly packed surfaces (e.g. layers in graphite or inter-tube space in the bundles) leave no room for H_2 as well (the formation energy is high/positive, that is "binding" energy is formally negative). In our search for optimal middle-range separation (0.5 - 0.7 nm), where the potential wells would overlap synergistically, we considered foam-type structures that can be obtained by coalescence. **Fig. 2** here shows simulation of coalescence on the SWNT-crossing, representing an elementary cell of such foam (note the benefit is that both interior and exterior of the original tubes become available).

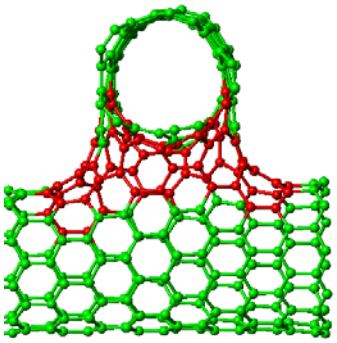

Fig. 2. Welding of two perpendicular SWNT.

As a step prior to modeling of spillover process (where catalytic dissociation of the molecular hydrogen leads to covalent binding of H) we performed electronic structure calculations of SWNT-H_n. Electronic structure computations were first performed with PM3 semi-empirical method. We observe the dependence of binding energy on the SWNT diameter; however there was no systematic dependence on chirality revealed so far. Overall lesson, verified further with accurate DFT calculations, was that in spite of curvature and even presence of topological defects, the H_2 binding remains insufficiently strong to store/retain the required amounts of hydrogen mass on either interior or exterior of SWNT.

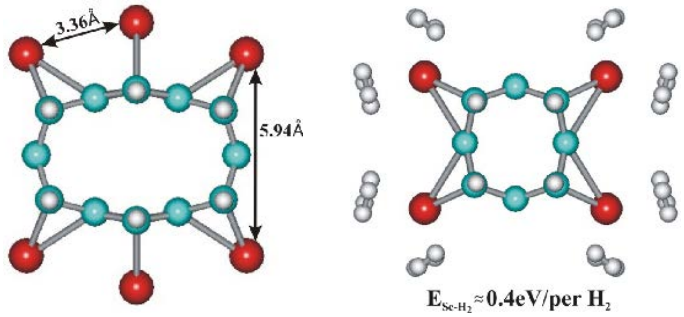

Fig. 3. Relaxed cross section geometries and binding energies for Sc-inhanced SWNT exterior.

Storage enhancement by intercalated metal elements was the other task-line of the project. For example, we considered Sc (**Fig. 3**) also shown as one of the efficient metals in NREL work (Zhao et al. PRL **94**, 2005). To further explore the feasibility and practicality of this appealing idea, we at Rice investigated the possibility of metal aggregation, how it can change (reduce) capacity for hydrogen, and how metalover aggregation (metal droplets) can be avoided. The latter is a critical problem that might be detrimental in case of some metals, but not so serious for others. Calculations show that Ti is more "wetting" to the tube and therefore likely not to roll into particles. We have computed the energies of metal-SWNT binding, distortions of the nanotube (**Fig. 3**, shown are the cross-sections), and the binding energies of H_2 to these systems.

Clustering of metal atoms and its effect on metal assisted hydrogen storage. We first investigated, with results shown in the **Fig. 4** below, the **(a)** diameter and **(b)** chirality angle dependence of binding energies of single Sc atom on SWNTs. **(c)**, **(d)**, and **(e)** show the optimized structure of Sc@(8,0), (6,2) and (4,4) SWNTs.

Fig. 4

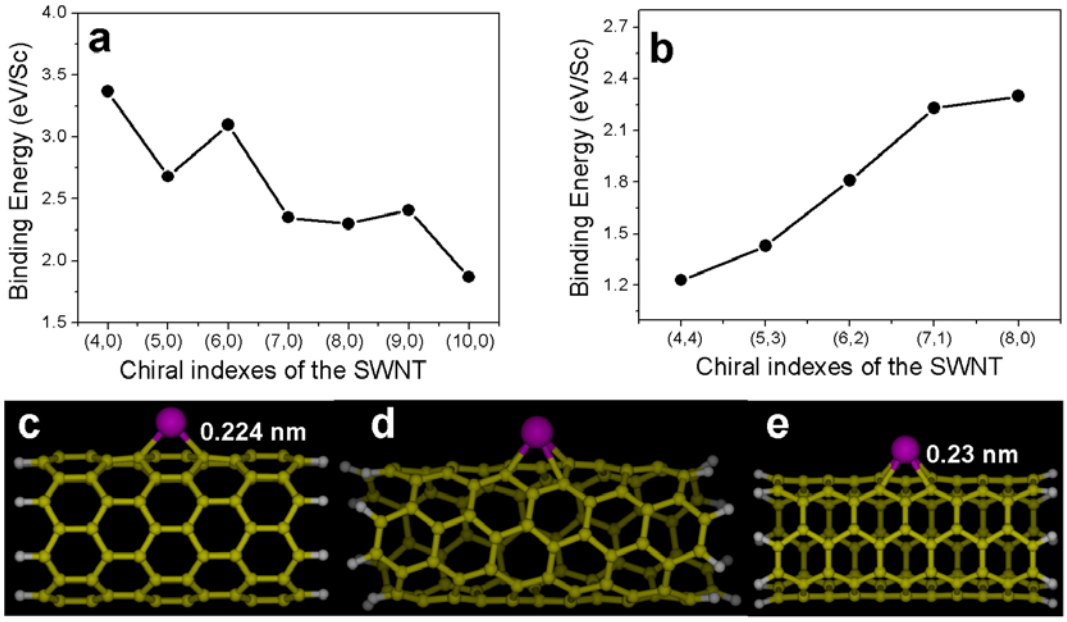

Then we accurately computed the binding energies of Sc and inter-atomic Sc-Sc distances on the surfaces of graphene and selected nanotube (8,0) clusters. Shown just below in **Fig. 5** is the optimized by Becke98/6-31G method structure of nanotube (8,0) cluster with 1, 2, and 4 of Sc atoms and 4, 5, and 4 hydrogen molecules, respectively. This work was completed and in its comprehensive form published.

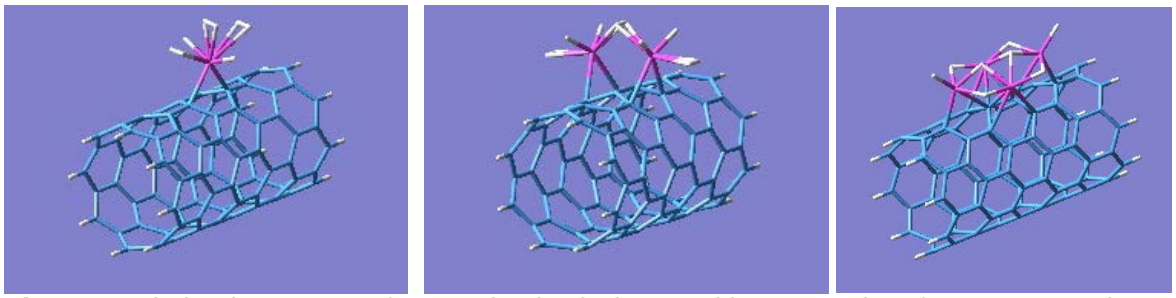

Fig. 5. Optimized structure of nanotube (8,0) cluster with 1, 2, and 4 of Sc atoms and 4, 5, and 4 hydrogen molecules, respectively.

It was also important to evaluate the kinetics of such possible aggregation. For this purpose, as now is also shown in the **Fig. 6**, we carefully computed the possible paths and barriers of Sc diffusion along SWNT (4,0) (up) and graphene layer (down) and corresponding barriers. The essential lesson from these studies is that decorating carbon scaffolds with sparse transition metal atoms could be of great benefit for hydrogen storage, but the practicality of this approach is limited by potential detrimental aggregation of metal into larger particles, therefore losing the ability to form Kubas type bonds. The most promising of all candidate metals appears to be Ti, due to its good ability to wet the carbon and consequently the thermodynamic driving force towards aggregation is reduced.

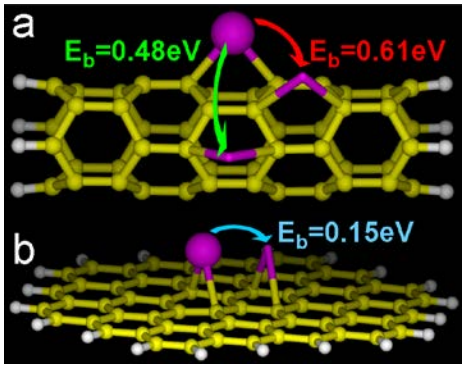

Fig. 6. Computed binding and diffusion barrier of Sc on carbon.

Identify 3D carbon nanostructures, including those with chemical enhancement groups, for best H-adsorption.

To find a configuration or a class of configurations able to bind molecular hydrogen significantly better that SWNT, studies suggested that the concurrent attraction to more than one wall can double the binding energy. Detailed analysis in our group and elsewhere suggested that the optimal spacing between the carbon walls must be 0.7-0.8 nm. This eventually led us to propose a concept of 3D-structures (cross-linked or foams). We further made progress in identifying their best geometry for storage. For example, the simple array of covalently linked carbon tubes appears to be better with mono- than with double p-phenylene cross link, in the **Fig. 7a** below.

For the foams, we have identified kinetic path to the cross-welding of nanotubes (or VANTA material), which shows how the nano-foams can be

engineered via physical processing. The foam has nanometer pores and channels, its entire surface (~2600 m^2/g) is accessible, it is lighter than water (~0.9 g/cm^3), and it has excellent thermal conductor advantageous for thermal management (and it is metallic). We have computed the binding energy landscape within the foam (b) in the **Fig. 7b** below.

Fig. 7a

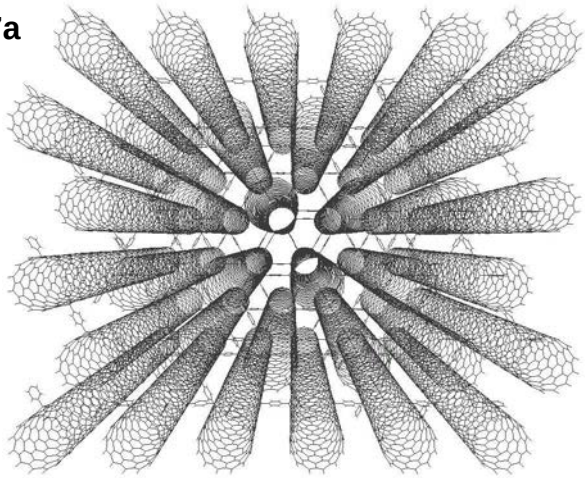

Fig. 7b

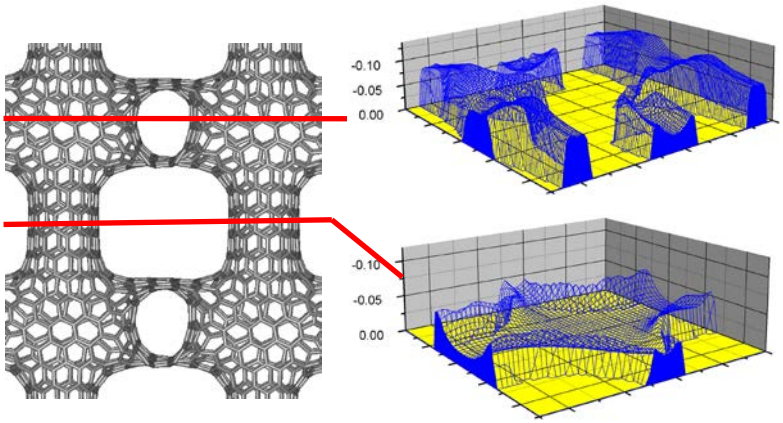

As extension of this work, we have performed precise H-C frequency computations, in order to determine the expected signature for different hydrogen binding positions of different curvature(s) and to help our partners at NIST to recognize the features in their planned neutron-scattering experiments, now published, Ref. 11.

<u>Production of SWNT by the “carpet growth” process that is optimal for molecular hydrogen adsorption, in the form of Vertically Aligned NanoTube Arrays (VANTA)</u>

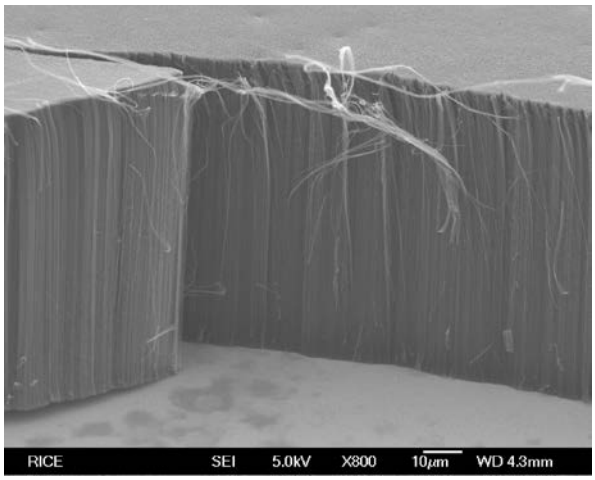

Fig. 8. Example of as grown VANTA, vertically aligned nanotube array.

Studies of the Rice HiPco SWNT production reactor were carried out with a different hot gas cold gas mixing geometry that maximized the reaction volume near the mixing zone. This resulted in approximately a 20% increase in SWNT production rate. Fluid flow calculations were also carried out to model gas mixing in the reaction zone in order to guide further changes in geometry. Surface area measurement indicated surface areas of the order of 1500 m^2/gram; however, hydrogen adsorption was too weak, preventing significant hydrogen adsorption at room temperature.

At this time, a concurrent discovery at Rice, clearly demonstrated that SWNT can be grown in vertical arrays as small diameter tubes (0.8-3 nm). A typical vertical array is shown in the **Fig. 8** SEM image. The chemistry of the growth method suggested that the diameter of SWNT can be made even smaller with less variation in diameter. The thickness of the arrays can be on the order of 0.5 mm. The opportunity to produce high density vertical arrays of SWNT with optimized diameters for H_2 adsorption appeared promising for hydrogen storage. The vertical arrays are in actuality a collection of small bundles of SWNT. Optimization of available surface area could be achieved by exfoliating the small bundles with oleum and incorporating a nanoparticle, light metal salt, or fullerene, as a spacer between SWNT. It is also possible to do oxidative opening of the ends of the SWNT and sidewall puncturing and cutting to increase gas access to the interior of the SWNT. Optimization of vertical array growth to achieve the smallest possible diameters was carried out.

Production of high surface area SWCNT arrays

Studies were carried out to optimize the production process of vertically arrayed SWCNT for best performance in hydrogen adsorption. A long range goal was to determine SWNT types (diameter, chirality, metal-enhancement) for H-adsorption.

The technical barrier that was addressed was the role of catalyst concentration and ability to control produced SWNT type. Production of SWNT by the “carpet growth” process (vertical array growth), that is optimal for molecular hydrogen adsorption, was systematically studied and improved.

Carpet growth: The Rice University process to make SWNTs utilized rapid heating in the presence of atomic hydrogen to lower barriers to SWNT nucleation in growth of carpets. The atomic hydrogen is generated with a hot filament in a fast flowing low pressure stream of hydrogen. This results in optimum SWNT nucleation before the nanometal iron catalyst particles are able to coalesce into larger particles.

This also leads to higher surface coverage's of SWNT than is possible with slower heating.

We have shown that atomic hydrogen is only required during the nucleation stage where its most important role is the reduction of the metal islands to the zero-valent metallic state that rapidly reacts with an acetylene carbon source. With atomic hydrogen, nucleation can be carried out at a low temperature (550^{o}C), which minimizes the surface mobility and coalescence of the nanometal particles. Continuous growth can be carried out at higher temperatures in the 700 to 800^{o}C range for periods of minutes to hours depending on the desired length of SWNT. Growth rates are typically in the 2-5 micron/minute range. This work demonstrated growth rates in the 20-30 microns/minute. Carpets have been sidewall functionalized with C-12 alkyl groups. This provides a baseline for comparison to sidewall functionalization with other groups that contain metal chelating groups. Attempts to produce specific types of SWCNTs did not prove to be possible. Hydrogen storage on unfunctionalized carpets proved to be similar to that for HiPco produced SWCNTs.

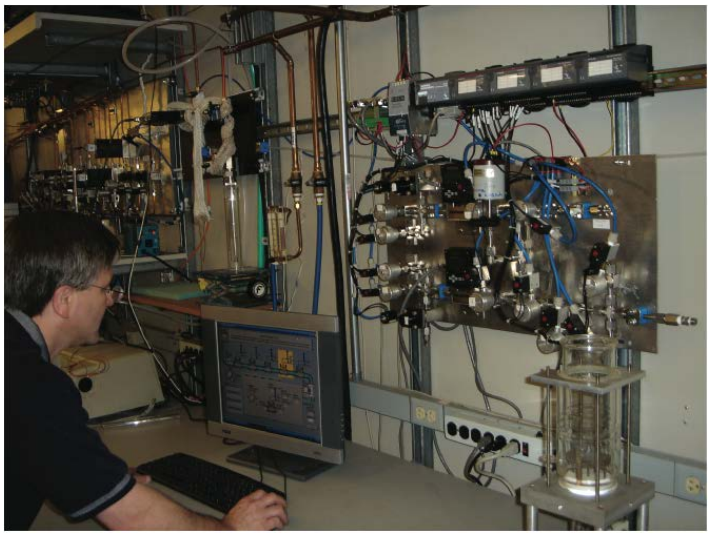

Fig. 9. Partial view of the valve control system of the fluorination apparatus at the carbon nanotube laboratory (Co-PI Hauge).

Super-acid enhanced hydrogen storage systems

This project studied the use of elemental fluorine and boron trifluoride doped high surface area carbon based materials for hydrogen storage. A direct elemental fluorination reactor was designed and constructed with the ability to add another gas such as boron trifluoride and other strong Lewis acids. The system is software controlled with the valve control system shown in the adjacent photo in **Fig. 9**. The thrust of this research was to enhance the binding of H_2 by introducing charge into the carbon lattice by removing charge from the carbon lattice to a highly stable bulky superacid anion that also acts as a spacer between carbon structures. This differed from other experimental work at Rice in that our main objective was to enhance hydrogen binding by increasing the charge state of the carbon lattice simultaneously with a bulky superacid anion spacer rather than focusing on the development of a 3D-engineered lattice for optimum hydrogen adsorption.

High surface area carbon obtained from other collaborators and vertical arrays of single wall carbon nanotubes (VANTAs) were converted into solid superacids by direct fluorination and subsequent reaction with a strong Lewis acid such as boron trifluoride. The aligned nature of VANTAs enhances gas transport into the array and

their length provides high thermal conduction along the aligned direction. Their aligned nature also lends itself to insertion of bulky anions.

Parameters for best growth of VANTA nanotube scaffolds were defined and VANTAs made available for addition of electronegative groups for enhanced H_2 adsorption. A variable temperature reactor was built and tested for controlled exposure of samples to fluorine and boron trifluoride. One gram samples were converted to a carbon nanotube salt and tested for hydrogen uptake in collaboration with NREL and Air Products Co. Tests of hydrogen uptake did not indicate a significant increase of hydrogen storage over unfluorinated materials.

To summarize:

- Parameters for best growth of VANTA nano-electronegative groups were optimized for enhanced H_2 adsorption.

- A variable temperature reactor was built and tested for controlled exposure of samples fluorine and boron trifluoride.

- One gram samples were converted to a carbon nanotube salt and tested for hydrogen uptake in collaboration with NREL and Air Products Corporation Center-partners.

- An upgrade of the direct fluorination reactor resulted into a capable/operational direct fluorination facility. High surface area samples provided by Cal Tech were exposed to fluorine and boron trifluoride and returned to Cal Tech for evaluation of hydrogen bonding behavior.

- Adsorption isotherm of MSC-30 sample BF_3/F_2-treated at 100^oC (wt gain due to F is 19 %) is in the **Fig. 10a**. Inset shows the isosteric heat as a function of surface excess adsorption. Limiting zero-coverage adsorption enthalpy is approximately 6.1 kJ/mol, consistent with that of pristine MSC-30.

- For comparison, **Fig. 10b** shows the adsorption Isotherm of pure MSC-30 (3350 m^2/g). Inset: isosteric heat. The zero-coverage enthalpy for MSC-30 was approximately 6.2 kJ/mole. *Adsorption data provided by Channing Ahn, Caltech.*

- Negative but important lesson from the initial studies indicates that converting a high surface carbon substrate to a superacid with charge separation stabilized via BF_3 complexation does not noticeably enhance the adsorption of hydrogen.

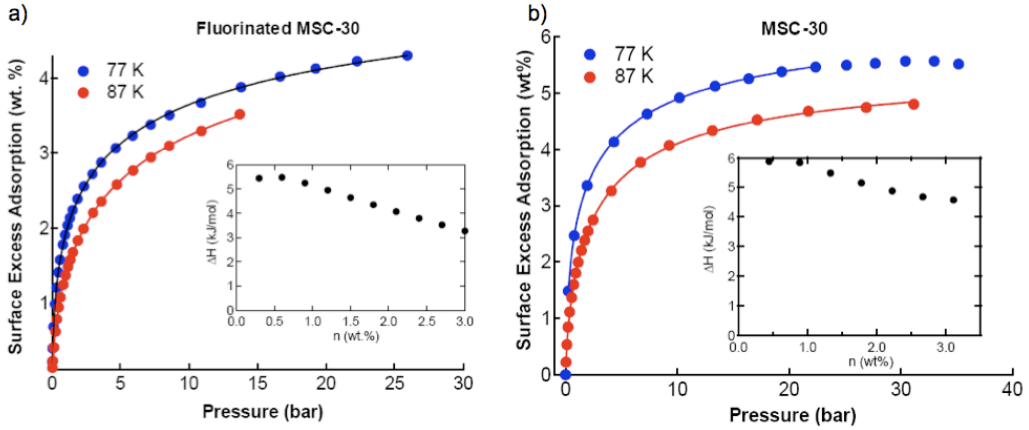

Fig. 10. Adsorption isotherms for fluorinated (a) and pure MSC-30. Insets in both (a) and (b): adsorption enthalpy changes.

Rapid simulation assessment of H_2 physical-sorption capacity, using GCMC methods, including quantum corrections thinness

Hydrogen storage in the three-dimensional carbon-foams can be analyzed using classical grand canonical Monte Carlo (GCMC) simulations, to quickly assess if storage capacities of the foams meet the targets. The pore sizes in the foams can be optimized for the best hydrogen uptake. The capacity depends sensitively on the C-H_2 interaction potential, and therefore the results should be presented for its "weak" and "strong" choices, to offer the lower and upper bounds for the capacities. Furthermore, quantum effects on the effective C-H_2 as well as H_2-H_2 interaction potentials are considered. We indeed have shown that the quantum effects noticeably change the adsorption properties of foams and must be accounted for even at room temperature.

In case of 3D carbon nano-porous materials, we have shown that the pore size ~1 nm could be ideal for storage. Several 3D carbon foams were both experimentally produced and theoretically proposed. However, the experimentally synthesized foams often have very large pore sizes whereas theoretically discussed foams often lack any suggested way of making them. We focused on carbon foam achievable via a known welding technique from crossed carbon nanotubes. These foams are almost isotropic, stable, and mechanically nearly as stiff as steel in all directions. The abundance of pores in these foams makes them ideal for hydrogen storage, while their architecture is well defined and can be designed in a systematic manner. Even if not made directly in practice, such foams can be useful as a representative model-system for studying storage in practical nanoporous materials with usually known making-recipe and measured surface area but very little data about their atomic makeup (activated carbons, aerogels, nanoporous and amorphous carbons). With this in mind, we designed a series of 3D carbon foams using different SWNT, aiming to assess the volumetric and gravimetric capacities and to find the optimum storage. Grand-canonical Monte Carlo (GCMC) simulations were used, with the judicious choice of interaction potentials, to estimate the storage capacities under ambient conditions. The storage capacity of such foams is compared with the

optimally-separated CNT bundles. The mass densities and pore sizes are optimized for the hydrogen uptake. Due to lightweight of H_2 and low storage temperature, the *quantum effects* on the C-H_2 as well as H_2-H_2 interaction potentials are considered and their consequences on the storage are evaluated.

Generation of foam structures

Carbon foams are designed by welding SWNT. In order to obtain foam an armchair and a zigzag SWNT of similar diameters are chosen. While the similarities in diameters ensure the uniformity of foams in x- and y-directions, the choice of different chiralities ensures the A-A stacking at the crossing interface-contact, when in the starting configuration the tubes are placed perpendicular to each other. The facing C-C pairs in the central part of the interface are brought to 1-1.5 Å, to the C-C bond length (that is pressed to each other, to initiate the welding-coalescence). If the spacing is too large, the connection cannot be built, while at too small distances the tubes fuse very quickly leading to a non-uniform "fat" neck, which is also undesirable. As a next step we construct a unit cell of foam via welding process. In each step, the most energetically preferred bond in the tube junction is rotated by 90° via Stone-Wales (SW) transformation, followed by relaxation of the whole structure. During the relaxation process, the tubes' edges are fixed to prevent them from becoming parallel to each other. The process continues until the neck becomes thick and a smoothly curved junction is formed. For the optimization process we used conjugate gradient method with the Tersoff-Brenner interaction potential for carbon. The computed energies of the structures at each step of the welding process are plotted below, **Fig. 11**. The letters mark the local minima and correspond to structures (**a-h**). Clearly, the junction formation is thermodynamically favorable, provided sufficient pressure, and should be kinetically achievable at elevated temperature and especially when irradiated.

We note that while topology does require no less than 12 heptagons upon the neck formations, a few excessive defects (pentagons and accordingly extra heptagons) emerge in the welding process. The relaxation can be continued until all the extra defects are removed and the junction with 12 heptagons is formed, following the Euler's rule.

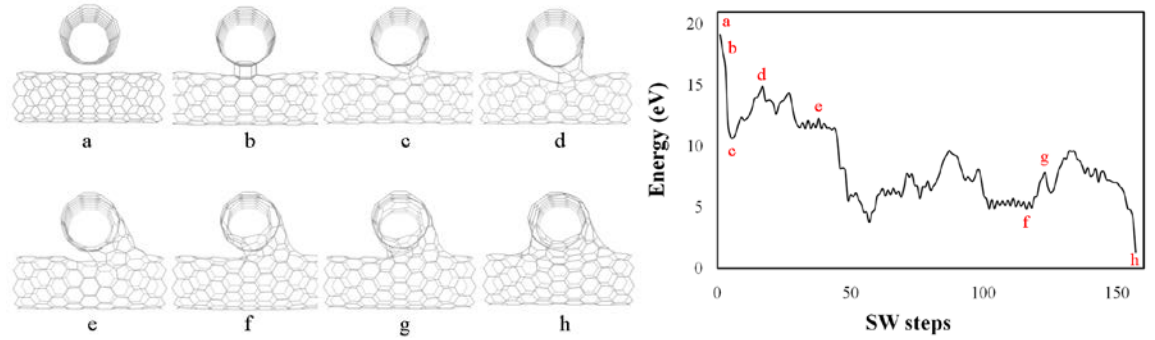

Fig. 11. Atomistic structure evolution during SWNT welding (a-h) and their corresponding energy changes versus the number of Stone-Wales transformation steps (right).

Foam families: In attempt to systematically compare the storage capacities of different foams, we generated two families of foams: one *isodensity*, with constant mass density, and another one geometrically-*similar*, where tubes, pores and channels all scale up roughly in proportion. It is summarized in the graphical Table below, inside **Fig. 12**, below.

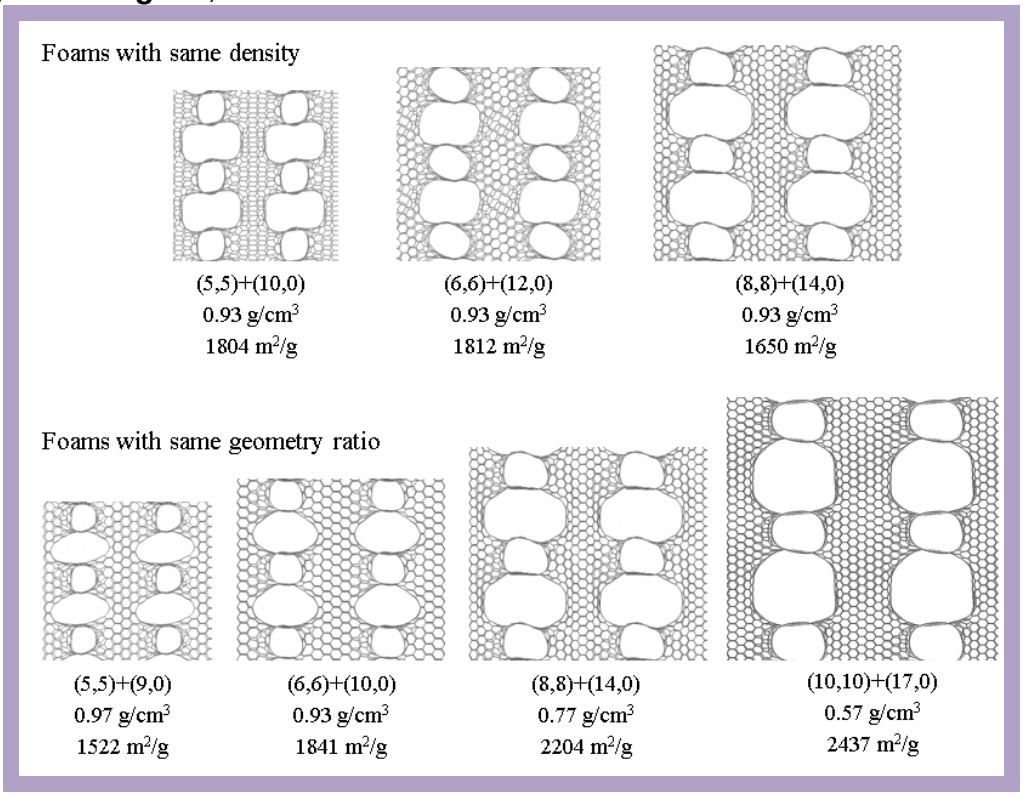

Grand-Canonical Monte Carlo simulations

The storage capacities are calculated using Grand Canonical Monte Carlo (GCMC) simulations, with empirical interatomic potentials. GCMC is a powerful technique to estimate the ambient condition storage by explicitly accounting for density fluctuations at fixed volume and temperature. This is achieved by means of trial insertion and deletion of molecules, H_2. At first, a random trail attempt is made for choosing between the particle insertion and deletion. In the case of insertion, a particle is placed with uniform probability density, whereas for deletion one out of N particles is randomly deleted. The trial is accepted or rejected according with their grand canonical weighting.

The simulations are carried out in 3D cells, with the periodic boundary conditions employed to exclude the surface effects. The positions of the C atoms of the foam are fixed. The energies of the H_2 adsorption sites were calculated classically. A typical simulation consists of 10^6 steps to ensure that an equilibrium configuration was reached, followed by 2×10^6 steps to evaluate the number of hydrogen molecules N_{H_2} in the considered volume. The simulations performed are at three different temperatures of 77, 150, and 298 K and in a pressures range of 0.01 MPa to 10.24 MPa (divided into 11 points). The center of mass of molecule is used to describe the position of H_2.

For the hydrogen storage the total capacities include also the hydrogen that would be there even in absence of the sorption materials. In order to get the more instructive metric of material-related adsorption storage, one defines *excess* capacity, which is the stored hydrogen in the system minus the storage in the same volume in absence of any sorption media. Resulting number of hydrogen molecules used to calculate the wt% and vol%.

Interaction Potentials

The storage capacity depends on the choice of C-H_2 interaction potential, and is sensitive to the C-H_2 binding energy. Such empirical potentials are obtained by fitting either experimental adsorption data or *ab initio* adsorption energy. In our work, we have selected two different H_2-C potential used extensively in the literature. This allowed us to analyze how much the variability in the potential affects the storage. One of the interaction potential has a 12-6 Lennard-Jones form (Wang *et al.*), with parameters chosen to fit the energy spectra from scattering experiments of H_2 physisorbed on graphite,

$$u(r) = 4\varepsilon[(\sigma/r)^{12} - (\sigma/r)^{6}],$$

where ε = 3.7 meV/molecule, σ = 3.0 Å. The other potential has an empirical LJ form proposed by Patchkovskii et al. (PNAS, 2005),

$$u(r) = A\, e^{-\alpha r} + C_6 r^{-6}$$

where A = 1100 eV/molecule, C_6 = −17 eV Å^6/molecule and α = 3.6/ Å.
In spite similarity in forms, the potential of Patchkovskii *et al.* gives a stronger C-H_2 binding and results in higher absorption, compared with the more conservative results obtained with the potential of Wang *et al.* Accordingly we call them strong and weak, and the storage capacities obtained by using these two potential offer a the *upper* and *lower* bound for expected realistic experimental range. For H_2-H_2 interactions we used the Silvera-Goldman potential, which treats hydrogen molecule as single particle with no rotational degrees of freedom. In a recent study it has been shown by first-principles calculations, that the configurations with different H_2 orientations have comparable absorption energy, which—together with rapid thermal rotational motion—justifies approximating the H_2 molecule as a single particle.

Quantum corrections

For the light molecule like hydrogen at low temperature the quantum effects can be significant. By considering the quantum effects in hydrogen isotopes it has been shown that heavier isotopes are adsorbed stronger than lighter ones. By comparing the thermal de Broglie wavelength of a particle of mass m, $\Lambda = (\beta h^2/2\pi m)^{1/2}$ where $\beta = 1/k_B T$, k_B being the Boltzmann constant and T the temperature with the mean pore size a, the validity of classical treatment can be tested. The classical treatment is justified only for the cases, where the ratio $\Lambda / a << 1$.

The quantum effects can be incorporated by elegant Feynman and Hibbs variational treatment, where a quantum particle of mass m is characterized by a Gaussian spread with a thermal quantum width Λ, around the particle center of

mass. The corresponding partition function of an assembly of N such particles can be expressed as

$$Z_{FH} = \frac{1}{N!}\left(\frac{2\pi m}{\beta h^2}\right)^{2N/2} \int ... \int d\bar{r}_1 ... d\bar{r}_N \times \exp\left[-\beta \sum_{i<j} U_{FH}(r_{ij})\right],$$

where

$$U_{FH}(r) = \left(\frac{24\pi\mu}{\beta h^2}\right)^{3/2} \int d\bar{R} U(|\bar{r} + \bar{R}|) \exp\left(\frac{24\pi^2\mu}{\beta h^2} R^2\right)$$

is the average effective potential between a pair of particles (reduced mass μ = m/2), incorporating the spread in position due to the uncertainty principle. An expansion of Eq. 2 leads to the accurate expression of the quadratic Feynman–Hibbs (QFH) potential:

$$U_{FH}(r) = U(r) + \frac{\beta h^2}{96\pi^2\mu}\left[U''(r) + \frac{2U'(r)}{r}\right],$$

where the prime and double prime are the first and second r-derivatives, respectively. C-H_2 and H_2-H_2 corrections depend on temperature, with the QC in C-H_2 being less significant. Effectively, quantum corrections add some repulsion as shown in **Fig. 13** below. There displayed are the C-H_2 and H_2-H_2 interaction potentials, purely classical (black), and incorporating the quantum effects at T = 77 K (red), 150 K (green) and 298 K (blue). The strong and weak potential choices for C-H_2 are shown separately. The quantum effects weaken the binding by the amount inversely proportional to T.

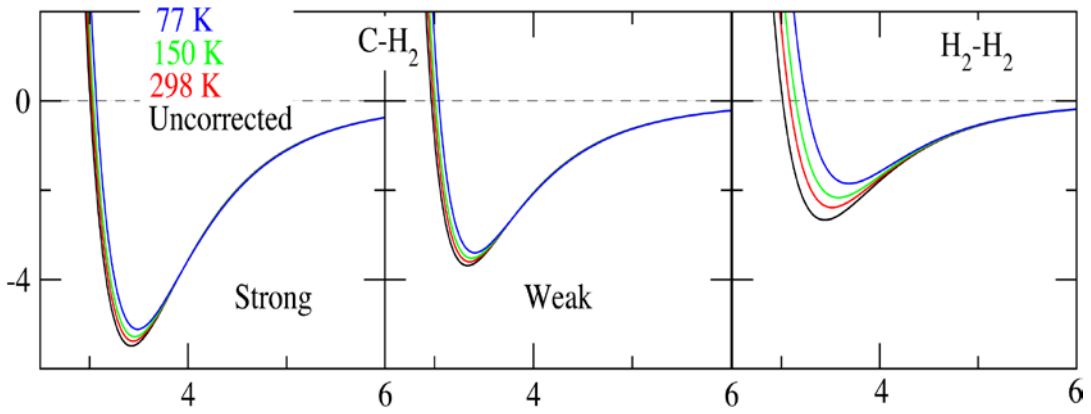

Fig. 13. Interatomic potential plots, for strong and weak C-H_2, and for H_2- H_2. Color coded are potentials with quantum corrections, at T = 77-298 K.

Accessible surface area

Surface area is an important and commonly used parameter, related to the adsorption capacity of the media. Generally, surface areas are measured by Brunauer, Emmet, and Teller (BET) method via N_2 adsorption isotherms. Due to differences in the effective size of the N_2 and H_2, the BET surface area calculated via N_2 adsorption is not very accurate for the purpose of hydrogen storage. We calculate the accessible surface area (ASA), which is geometrically obtained by "rolling" a probe molecule along the surface of the porous media. By choosing the diameter of

the probe molecule same as of adsorbent, a more relevant estimate of surface area can be obtained. We chose H_2 as probe molecule to estimate the ASA, which are given in the chart of configurations in **Fig. 12** above.

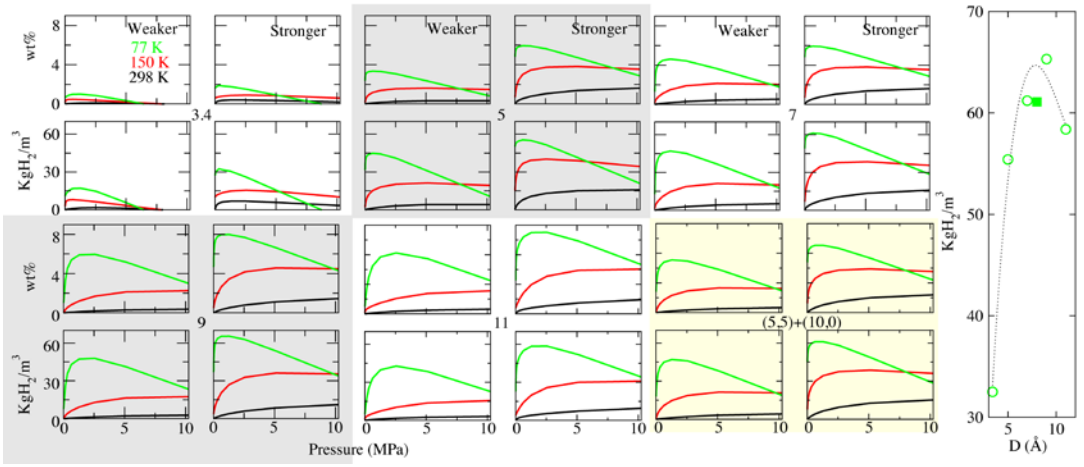

Fig. 14. The excess volumetric and gravimetric foam capacities versus P and T, for the *weaker* and *stronger* attraction (H_2 - C) potentials.

After putting the necessary "components" above together (foam structure generator, interatomic potential, quantum corrections, and GCMC), we compared the storage capacity of selected foams with the well-spaced same-diameter nanotube bundles. For this, we choose one foam previously generated in our group from the crossed (5,5)+(10,0) nanotubes (we use symbol "+" resembling the cross-orientation of the precursor-tubes). The bundles are generated by packing the (10, 0) nanotubes in a triangular lattice, and varying the wall-to-wall distance (D) within a bundle series. The excess volumetric and gravimetric capacities of these bundles are shown in **Fig. 14** above. The gravimetric fraction increases monotonically with the increasing tube-tube separation; however, the volumetric capacity peaks at D = 9 Å. The metrics for the foam are also shown. The maximum volumetric ratio in the foam is obtained at T = 77 K and 1 MPa, which compares very well with the corresponding maxima of the tube bundles as shown in **Fig. 14**, right. Although they have similar storage capacity, to synthesize a bundle of well-aligned tubes with uniform spacing of 9 Å is unfeasible. Normal tube-tube distances in the bundles are ~3.4 Å, and the storage capacity is far less than the foams. The superiority of foams over the tube bundles is due to the better architecture, which ensures the accessibility and uniformity of the pores. Partial advantage is also from the availability of better attraction sites for hydrogen around the neck area of the foams, due to enhanced curvature. Shown in **Fig. 14** data also demonstrate the effect of the two interaction potentials used in this study. Clearly, due to *weaker* C-H_2 binding strength in the Wang potential, the wt% and density of adsorbed hydrogen is systematically lower than the corresponding adsorption result from the "*strong*" Patchkovskii potential. As expected, these results show that the choice of interaction potential is of paramount importance. Due to the lack of experimental data for adsorption of H_2 molecules on foams, the accuracy of these potential cannot be easily validated. However, the results obtained from these

two potentials can serve as range in which the experimental value will lie. Therefore here we include the storage data obtained for both potentials.

Besides being a good media for hydrogen storage, 3D carbon foam offers an opportunity of generating structure with the desired pore sizes. This can be achieved by the adequate choice of the tube diameter and the separation between the necks. A series of foams can be obtained by the varying these parameters. Here we choose two different foam families as discussed above and shown in **Fig. 12** (page 13).

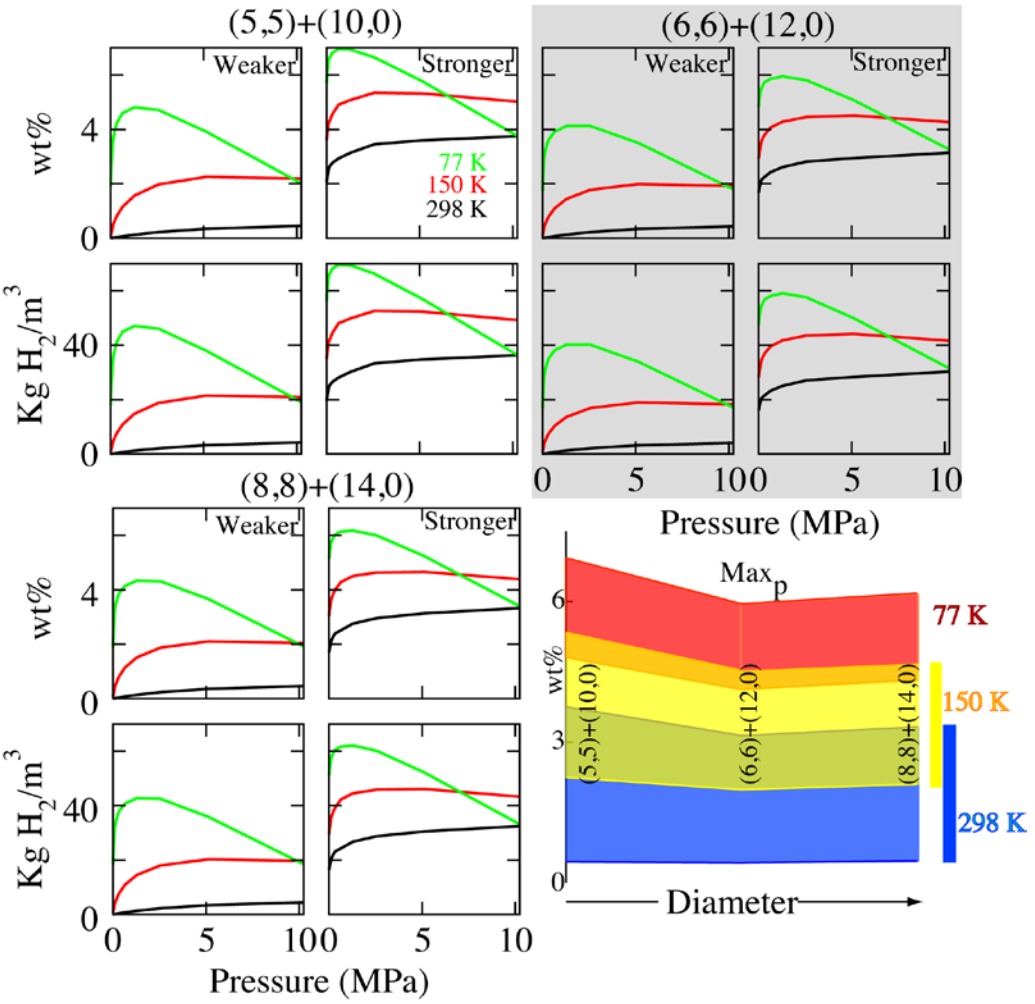

Fig. 15. Gravimetric and volumetric capacities for different foams of the iso-density set, and potentials. Bottom-right: the maxima obtained for different foams at different P, T.

The storage capacities of the foams with the same mass density were evaluated and also present graphically (see **Fig. 15**). In this isodensity family the diameters are varied while keeping the mass density of the foam material constant. We generated three such foams namely (5,5)+(10,0), (6,6)+(12,0), and (8,8)+(14,0). The choice of chiralities minimizes the difference in the diameter of the crossing tubes, to ensure the uniformity of the pores. The gravimetric and volumetric storage capacities peak for different types of the foams, respectively. The maximum gravimetric capacities obtained for these foams at different temperature and

pressure are displayed in the same figure below. Gravimetric capacity peaks for the (6,6)+(12,0) foam as shown at the right-bottom. This must be due to the optimal distances between walls of the precursor-tubes as well as between the formed necks. These parameters are close to 1 nm, which is optimal for storage capacities.

We further studied the adsorption of H_2 molecule in the other family of the foams, where the pore sizes are varied in the geometric proportion. Four such foams were generated by the method described in the previous section. The structures are shown in the lower panel of **Fig. 12** and the corresponding storage capacities are shown in the 16-panel **Fig. 16** below. The storage capacities show systematic behavior. The trend for *maximum* (over P, T) excess gravimetric and volumetric capacity is shown in **Fig. 17**. The gravimetric % increases monotonically, however, the volumetric measure peaks again at the (6,6)+(10,0) foam. The volumetric as well as gravimetric capacities follow the similar trend as ASA/volume and ASA/g, respectively, the upper panel of the figure. This is an important connection as the foams can be optimized by measuring surface areas per volume before doing actual hydrogen adsorption experiments.

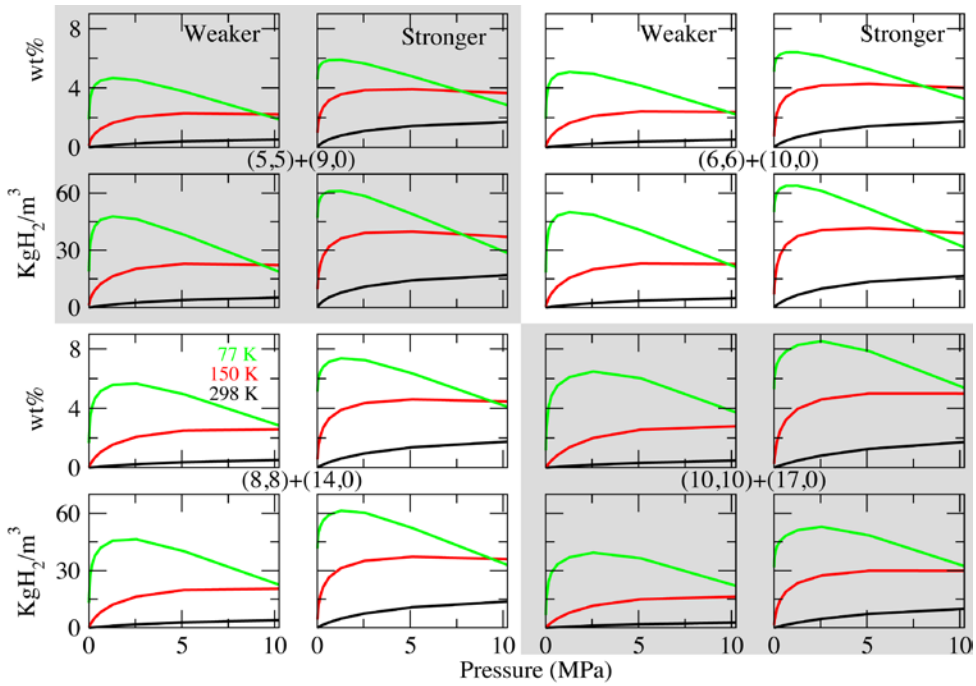

Fig. 16. Gravimetric and volumetric capacities for the geometrically–proportional foams, at different P, T and potentials.

Finally, for the lighter molecules where the de-Broglie wavelength could be significant, inclusion of the quantum effects are necessary. We incorporate the quantum effects in the interaction potentials. With the inclusion of the quantum corrections the effective interaction potentials become temperature dependent. The quantum corrected C-H_2 (both strong and weak) as well as H_2-H_2 Silvera-Goldman potentials are computed. The effective radius of the H_2 molecule increases at lower

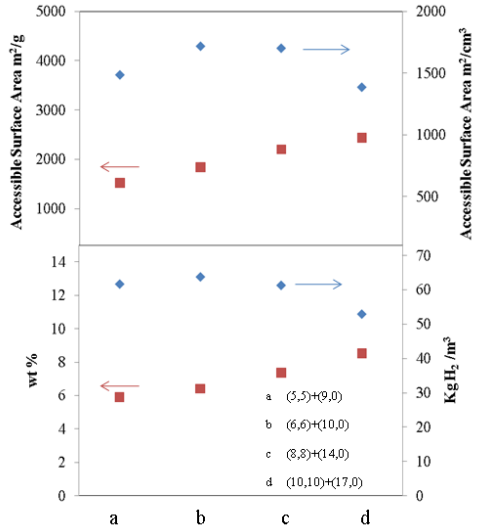

Fig. 17. Top: accessible surface area per volume and per gram. Below: maxima of volumetric and gravimetric capacity.

temperatures essentially reducing the depth of the attractive part of the potential. This reduces the storage capacity of the foams (or any other adsorbing carrier).

The storage capacities of foams with the quantum corrected potential are shown in the **Table** below. The quantum corrections reduce the storage capacity particularly at low temperatures. The table shows the overestimation of the storage due to neglect of the quantum effects. As expected the decrease is most significant with the decreasing temperature and increasing pressure. The hydrogen uptake can be reduced as much as by 24% at 77K. The classical results are more accurate at increasing temperature, but the consequences of the quantum effects still should not be neglected. Even at room temperature the storage is classically overestimated by as much as 7%. Furthermore we also analyze the sole effect of neglecting the quantum correction in H_2-H_2 potential. As can be seen from the Table major corrections are due to quantum effects in H_2 –H_2 interaction potentials. Therefore, inclusions of quantum corrections are important to make realistic comparisons with the experimental storage capacities.

Classical overestimates by (%)			
	C-H_2 with QC	C-H_2 and H_2-H_2 with QC	
T	wt % total (at P)	wt % total	wt % excess
298 K	2.6-3.1 (~10 MPa)	5.6-5.8	7.8-12 (10 MPa)
150 K	3.2-4.0 (~10 MPa)	12-13	14-16 (~5 MPa)
77 K	3.1-5.2 (~10 MPa)	18-23	21-24 (~1 MPa)

Table: Storage capacity overestimates (in %) of purely classical simulations relative to the corrected for quantum effects, for (5,5)+(10,0) foam.

We design a series of the 3D-foams using welding algorithm-process, which has its analogues in experiments. We compute the storage capacities of such foams using classical GCMC simulations. These simulations were performed with the two selected types of C-H_2 interaction potential (*weak* and *strong*), which sets the range for the storage capacity prediction. Storage parameters depend sensitively on the choice of the interaction potential. For comparison, we also simulate the storage

capacity of the idealized open nanotube bundles with varying tube-tube distance. We find the storage capacities of the foams to be comparable to the similar diameter nanotube bundles. Two families of foams are generated, one with constant mass density (iso-density) and another of nearly unvarying shape (geometrically similar). The foams are optimized for best storage capacity within both of the families. Furthermore, we study the consequences of quantum effects on storage capacities. The quantum effects are incorporated in the interaction potentials via Feynman - Hibbs formulation. The quantum effects noticeably reduce the storage capacity and must be incorporated in order to make realistic predictions for the experimental systems. The foams can serve as a model for various nanoporous materials whose atomic structures are often poorly defined while their making-recipes and the surface areas are known. Model foams with the desired surface area can be readily generated and then their storage capacity can be quantitatively evaluated at arbitrary pressure and temperature. Furthermore, as soon as the structure is selected, the study can be extended to the diffusion and transport, including thermal, to also evaluate non-equilibrium, kinetic performance of the material. Foams thus can provide an indirect method for theoretically assessing the feasibility of and performance of carbon nanoporous materials.

Comprehensive model of spillover mechanism, including H chemisorption to carbon receptor and functionality of the metal catalyst

Spillover, H-receptor thermodynamcs

Hydrogen spillover on light *receptor*-substrate, recently of great interest for energy storage, can be recasted as a process of phase nucleation in a solid-state reaction, $Rec^{solid} + H_2^{gas} \leftrightarrow (H{\cdot}Rec)^{solid}$. State-of-the-art atomistic calculations, from individual chemisorbed atoms to small compact clusters and to larger islands, can be bridged remarkably well with the macroscopic-continuum description of a new phase island-nucleus, whose energy can be decomposed into its “bulk” Gibbs formation potential, and the interface boundary energy. This allowed us to estimate the critical nucleation size and barrier, at arbitrary pressure and temperature, and shows a feasible path to 7.7 wt% hydrogen content by reversible spillover at nearly ambient conditions.

The term (*hydrogen) spillover* has been defined decades ago as transport of active species (*e.g.* H) generated on one phase (*activator*, Act) to another phase (*receptor*, Rec) that would not normally adsorb these species. Common in heterogeneous catalysis, the typical activator is metal and receptor can be a metal or metal oxide, $H_2 \text{—}^{Act}\text{—>} 2H$, H + Rec —> H@Rec. While the catalyst does reduce the activation barrier, it cannot change the requirement for overall process H_2 + Rec —> 2H@Rec to go thermodynamically downhill: hydrogen binding ε_b to the receptor must be stronger than its binding $\frac{1}{2}E_{H_2}$ within molecular H_2. Typically, the number of adsorbed H-atoms exceeds that of activator by orders of magnitude, and approaches the number of the receptor atoms. This feature makes the spillover so attractive for hydrogen storage: If receptor can be made from light elements, notably carbon, then the gravimetric fraction of the “spilled” hydrogen might be large and come close to the practical goals set by the Department of Energy, in the use of hydrogen for onboard energy storage.

Recent observations demonstrated that atomic hydrogen can bind reversibly (that is be stored) to nanostructured carbon. In experiments with cold hydrogen plasma, it is important to note the high degree and yet reversibility of hydrogenation; in this case initial hydrogen is already in active atomic form and the positive energy ε_b = 0.7 - 0.8 eV of its binding to carbon (nanotube) is enough to make chemisorption thermodynamically favorable. In contrast, in spillover experiments the source is molecular hydrogen, and thus the 0.8 eV affinity to carbon appears to be far insufficient to overweigh the strength of H_2 molecule ($\frac{1}{2}E_{H_2}$ = 2.3 eV). Seemingly, such uphill change in energy could not be reconciled with the simple picture of H_2 dissociating on catalyst and then the H atoms diffusing all over the receptor. This posed a question of what configurations of chemisorbed hydrogen can be energetically favorable, how they can be reached, starting from initially pristine receptor, and is it possible to suggest a simple picture of transition into these "storage" states?

To this end, we have systematically considered small groups of H chemisorbed on graphene (**Fig. 18**), starting from the 1, 2, 3, *etc*. atoms and towards larger clusters, using *ab initio* methods. Although single H binds to graphene weakly, the binding dramatically strengthens as chemisorbed clusters begin to form, with major factors being proper pairing in such alternant hydrocarbons, and the compensation of pyramidalization if the adjacent C-atoms get hydrogenated from the opposite sides of graphitic plane. The best binding is achieved for compact islands comprised of fully hydrogenated hexagons. Remarkably, the islands' energy can be characterized by two distinct contributions: the wetting energy, proportional to the island area ~l^2, and the boundary energy proportional to the island perimeter, ~l. This invokes an interpretation of spillover process as nucleation and growth of a new phase, with the free energy ~($-l^2 + l$), and accordingly defined critical size l^* of the nuclei and the nucleation barrier ΔG^*, calculated at different thermodynamic conditions.

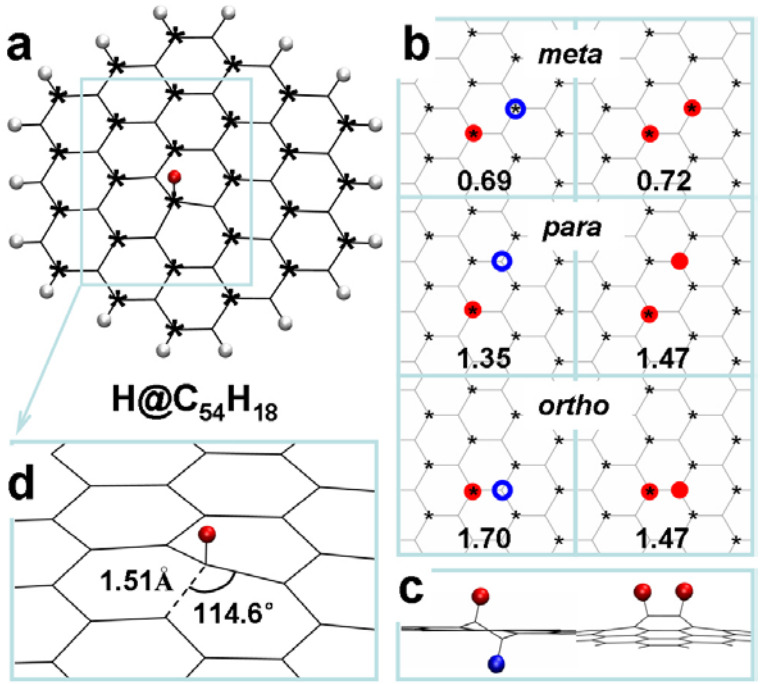

Fig. 18. Structures and binding energies energy of atoms H chemisorbed on $C_{54}H_{18}$, model substrate-receptor.

Relative to molecular H_2, the formation energy for spillover/chemisorption is $\varepsilon_{so} = -\varepsilon_b + \frac{1}{2}E_{H_2}$. Positive means that chemisorption is energetically upward, unfavorable; media with very small negative still cannot retain hydrogen efficiently at ambient conditions (as often is the case for physisorption). On

the other hand, too negative ε_{so} (*e.g.*, < -0.3 eV) makes adsorption irreversible, unless at high temperature. Therefore, for good storage ε_{so} must lie within -0.6 eV < $2\varepsilon_{so}$ < -0.2 eV. Since this range is rather narrow, the accuracy of calculations can affect the conclusion whether H can be feasibly stored on carbon or not. After careful consideration and comparison of the methods and basis set options, we chose to conduct all the computations with PBEPBE/6-31G** within Gaussian03 package. Graphene was represented as either a polycyclic aromatic hydrocarbon cluster $C_{54}H_{18}$ (circumcoronene) comprising nineteen peri-fused benzene rings or an infinite layer, treated with periodic boundary conditions (PBC).

For a cluster of *n* chemisorbed hydrogen atoms, the average binding energy $\varepsilon_b(n)$ is defined as:

$$\varepsilon_b(n) = (E_g + n\cdot\varepsilon_H - E_{nH@g})/n,$$

where E_g is the energy of either graphene or its representative fragment (*e.g.* $C_{54}H_{18}$), ε_H is the energy of single H atom, and $E_{nH@g}$ is the total energy of hydrogenated graphene [for instance, the above mentioned binding energy of a single H corresponds to $\varepsilon_b = \varepsilon_b(1)$]. We compute these quantities to observe some trends and regularities in the strength of chemisorption.

Similar to benzene C_6H_6, the circumcoronene $C_{54}H_{18}$ has an alternant conjugated system of the sp^2 carbon layer. According to the perturbation molecular orbital theory, its atoms can be divided into two subgroups, one starred and another unstarred, **Fig. 18**. For an aromatic system like $C_{54}H_{18}$, the π electron of each starred/unstarred atom is paired with another π electron of an unstarred/starred carbon according to the pairing theorem. Adsorption of an H atom eliminates one π electron, thus such a system has odd number of π electrons, one of them unpaired, *i.e.* a radical. This raises the total energy, and thus the binding energy 0.79 eV of the single H is small, 1.5 eV less than $\frac{1}{2}E_{H_2}$, too weak to drive the spillover.

Adding another H to the carbon of opposite subgroup removes the radical state and thus lowers the energy. As shown, two H atoms are added in six nonequivalent configurations: *ortho*, *meta*, and *para*, with two options for each, either H's on the same side or on the counter-sides of graphene. In *meta*-configuration, both H's are linked to C atoms from the same subgroup, which creates two radicals and results to much weaker binding than in *ortho*- and *para*-configurations, **Fig. 18**.

Generally, minimizing the number of unpaired π electrons increases the binding energy. Since each π electron pair consists of one π electron from a starred carbon and another from an unstarred carbon, for a given number of chemisorbed H, the binding energy is best if equal portions of H atoms are bound to the two subgroups. An odd number of chemisorbed H atoms yield at least one unpaired π electron (radical) in graphene, destroying its aromaticity. Consequently, the energy increments ΔE_n for the oddth adsorbed H must be notably less than those for the eventh. The ΔE_n values for the H atoms from 1st to 6th do clearly show such oscillations, **Fig. 19**.

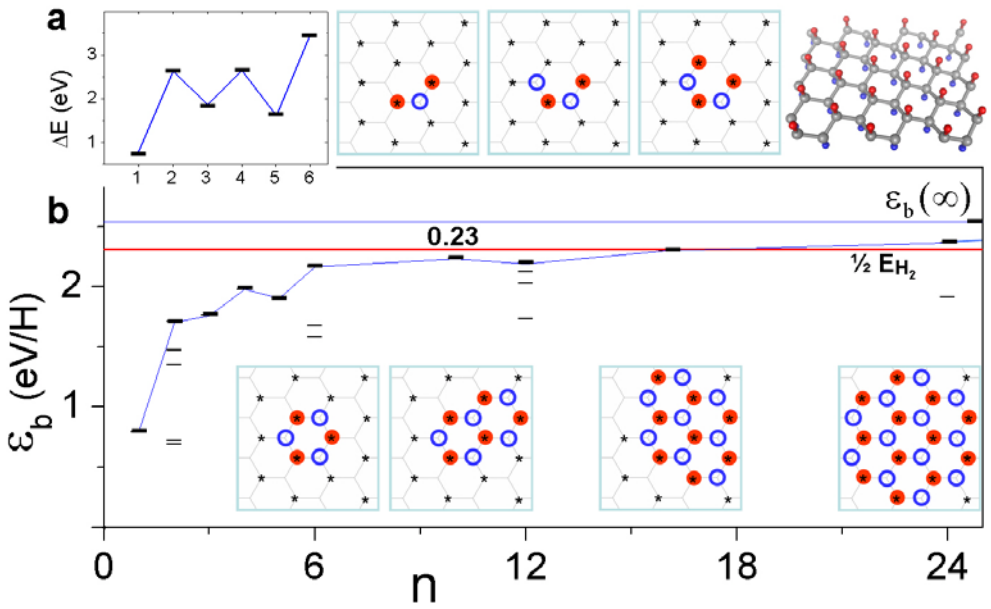

Fig. 19. Binding energies as a function of number of H atoms adsorbed display the aromaticity effect and closed six-ring preference for H chemisorbed on graphene.

Chemisorption of H alters the hybridization of the host C atom from sp^2 to sp^3. The C-C bonds between the sp^3-atom and its three nearest sp^2-neighbors are elongated to ~0.15 nm and the angles between them are reduced from 120° to 115°, while the hydrogenated carbon atom buckles off the graphene plane, in the course of pyramidalization. If two adjacent C atoms are hydrogenated from the opposite sides, the induced strains mutually compensate each other, reducing the energy. Such configuration is more stable than the one with both H attached on the same side. For example, the binding energy for the H atoms in *ortho*-configuration increases to 1.70 eV if they are in the counter-side configuration, from 1.47 eV if they are placed at the same side.

How such energetically favorable monolayer "diamond slab" on the right of the **Fig. 19** can be reached in the course of spillover, can be learnt by inspecting the data in **Fig. 19**. The formations with complete hydrogenated 6-rings are lower in energy and more stable than those with open rings. The 3.5 eV binding energy of the ring-closing 6th H-atom is much greater than of the 2nd or 4th (~2.7 eV). The configurations composed of complete 6-rings (*e.g.*, of 6H, 10H, 16H, and 24H@$C_{54}H_{18}$) have stronger binding than any others with incomplete 6-rings, *e.g.* 12H isomers. (This "closed-ring rule" for adsorbed H distinctly differs from the belt formation on a thin nanotube where large wall curvature apparently controls the morphology of hydrogenation.)

Tendency of the chemisorbed H atoms to crowd together brings about an important question whether a condensed 2D-island of H on graphene can be treated as a nucleus of a new phase, so that its energy is separable into the "bulk" and boundary (interface) contributions. One can distinguish three types of C-C bonds: those within pristine carbon sheet (connecting sp^2 atoms), those within fully hydrogenated graphene (between the sp^3 diamond type atoms), and the bonds tagged "23" (connecting sp^2 and sp^3 carbons) at the interface of hydrogenated and

pristine graphene. With this in mind, we plot the binding energies $\varepsilon_b(n)$ versus the fraction of border-type bonds n_{23}/n, for several optimized aromatic configurations, with H adsorbed on both sides. The data points follow the line $\varepsilon_b(n) = \varepsilon_b(\infty) - \gamma (n_{23}/n)$ strikingly closely, deviating by less than 0.03 eV, with $\varepsilon_b(\infty) = 2.54$ eV and $\gamma = 0.41$ eV. It shows that the total formation energy of a spillover-island can be decomposed into its "bulk" contribution proportional to the number of chemisorbed atoms n, *i.e.* island area, and "surface" term proportional to the number of border bonds $n_{23} \sim \sqrt{n}$, *i.e.* island perimeter/interface.

$$\varepsilon_{so}(n)\cdot n \equiv [\tfrac{1}{2} E_{H_2} - \varepsilon_b(n)]\, n = -[\varepsilon_b(\infty) - \tfrac{1}{2} E_{H_2}]\, n + \gamma \cdot n_{23} = -0.23\, n + 1.01 \sqrt{n}\ , \text{eV}$$

In the latter, we assume nearly circular island shape, to relate the number of perimeter bonds with the total number n of chemisorbed atoms, $n_{23} \approx \sqrt{6n} \sim l$. Integer n is formally treated as continuum variable proportional to island's area or radius squared, $n \sim l^2$. It is then easy to recognize in this equation a signature energy dependence $\sim(-l^2 + l)$ of a new phase nucleus. Furthermore, an important generalization follows if a fixed value of $-\tfrac{1}{2} E_{H_2}$ is properly replaced by a chemical potential $\mu_H(P,T)$ of diatomic H_2 gas, at arbitrary pressure P and temperature T. **Figure 20** below shows the Gibbs free energy $\Delta G(n) = -[\varepsilon_b(\infty) + \mu_H]\, n + \gamma \sqrt{n}$ of the "spilled-over" nucleus formation, as a function of its size n, computed for different T and P. First, the inset equilibrium diagram shows the conditions where either free molecular gas [at $\Delta G(\infty) > 0$] or a fully chemisorbed state [at $\Delta G(\infty) < 0$] is more favorable. It is in reasonable agreement with experiments of nanotube dehydrogenation upon raising temperature to a few hundred degrees. It also shows that chemisorbed hydrogen is favored at ambient conditions, so that sp^2-carbon can in principle serve as good spillover receptor. At the same time, more detailed $\Delta G(n)$ curves display significant nucleation barriers (distinctly different from the H_2 dissociation barrier, reduced by the metal catalyst) even at thermodynamically favorable conditions, reflecting the fact that chemisorption of a single H is too weak to overweigh the strength of molecular H_2. In contrast, when the source of hydrogen is the atomic form in cold plasma, μ_H is very high and the nucleation barrier vanishes.

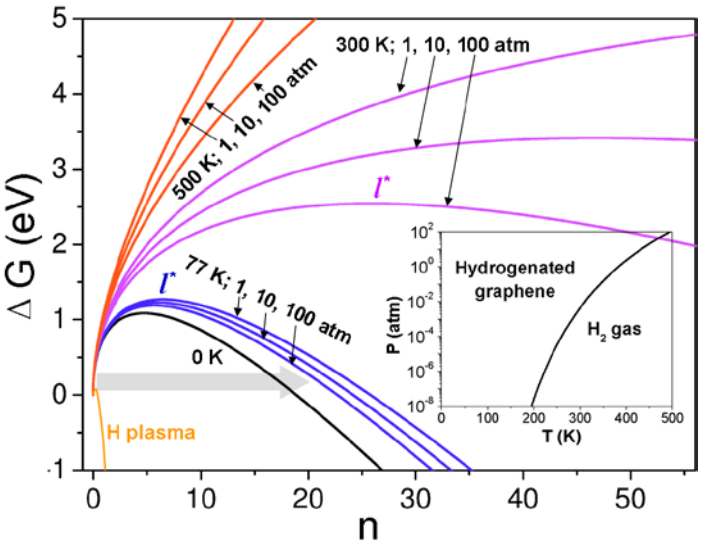

Fig. 20. Gibbs free energy of the formation of CH island of size n, at different P and T.

The barrier for homogeneous nucleation can be reduced by a nucleation seed, which essentially shifts the initial size towards the

larger numbers, beyond the critical n^* or dimension l^*, as indicated by the gray arrow. Possible nucleation centers can be lattice defects or the metal particle itself, in which case it plays dual role: as catalyst, to lower the reaction (H_2 dissociation) transition state, and also to reduce the nucleation barrier. One can also suggest in this context that the observed role of bridges, although not yet microscopically studied, can be in improving the contact of the catalyst center and effectively shifting the initial size to the larger values.

Our study revealed the thermodynamic aspects of molecular hydrogen gas spillover into the chemisorbed state on graphene. In the latter, H atoms tend to group into compact clusters, influenced by aromaticity rules and the pyramidalization strain compensation, so that the “magic” (lowest energy) clusters consist of closed six-hydrogen rings. Moreover, the energy of chemisorbed clusters fits surprisingly well a continuum model of an island, whose energy can be decomposed into its “bulk” and “surface” (island boundary) contributions. Computed Gibbs formation energy $\Delta G^{P,T}(n)$ plots show typical phase nucleation dependencies, with the nucleation barrier ΔG^* and the corresponding critical size n^* (or l^*) identified for arbitrary pressure and temperature conditions. Important applied aspect of this analysis is that the balance between the fluidic gas phase and the immobilized “7.7 wt% storage” phase can be changed in either direction by changing P and T not too far from the ambient conditions, thus permitting in principle reasonable refueling cycles. Needless to say, not considered above kinetics aspects, the processes rates and associated thermal effects remain important and require further investigation.

Role of metal cluster in spillover

Spillover almost always occurs in the presence of a catalyst and can be enhanced by using bridges between the catalyst and substrate. Following our previous study of metals on the surface of SWNTs, which shows that metals have very strong tendency to cluster, we have started working on the hydrogen uptake capacity of free small metal clusters. Pd_4 is chosen as the catalyst. We have addressed important aspect of spillover, with the details of hydrogen binding to the catalyst particle, which serves a gateway to the entire process.

The spillover phenomenon aspect, discussed above, leaves an open question about catalytic part of the mechanism and how an H atom binds to graphene instead of forming the thermodynamically preferred H_2. Using *ab initio* calculations we demonstrated that the catalyst saturation provides a way to the adsorption of hydrogen on the receptor by increasing the H chemical potential to a spillover favorable range. Although it is energetically unfavorable for the spillover to occur on a pristine graphene surface, presence of a phase of hydrogenated graphene facilitates the spillover by significantly improving the C-H binding. We show that thermodynamically spillover can occur, both from the free standing and from the receptor supported clusters. Further, the computed energy barrier of the motion of an H from the catalyst to the hydrogenated graphene is small (0.7 eV) and can be overcome at operational temperatures.

To reiterate, the spillover process involves the transport of an active species (e.g., H) formed on a catalyst onto a receptor that does not sorb the species under the same conditions. The most widely used catalysts for spillover of H-atoms on graphitic materials are Ni, Pd, Pt, and *3d*-transition metal atoms. Recently, several experiments have shown the enhancement of H_2 adsorption via spillover on activated carbons and MOF. Up to 4 wt% of adsorption has been reported for IRMOF-8 at 298 K and 10 MPa. Furthermore, it is empirically established, by the Center partners, that the spillover can be enhanced by adding so-called bridges between the catalyst and receptor. Although exact distribution and the binding sites of the H remain experimentally unspecified, it is reasonable to suggest that the best coverage of the H on graphitic substrates can be achieved when they are hydrogenated on both sides, and spillover is considered as a possible path to achieving it. Thus fully hydrogenated graphene would have stoichiometry CH, with 7.7 wt% of hydrogen, nearing the DOE goals. Even though the spillover of the H on graphitic surfaces was observed decades ago, it is still not well understood how an H binds to graphene, when it seems energetically more favorable to stay on the catalyst (or to remain in a molecular H_2 form in gas phase, as described in previous section). To better understand the spillover mechanism, with the goal to optimize its kinetics, it is important to compare the relative energy states of the hydrogen in its (i) dihydrogen gas form, (ii) at the metal-catalyst, and (iii) on the receptor-substrate, see **Figure 21**. The energy states available for H will depend on the degree of saturation, or substrate coverage.

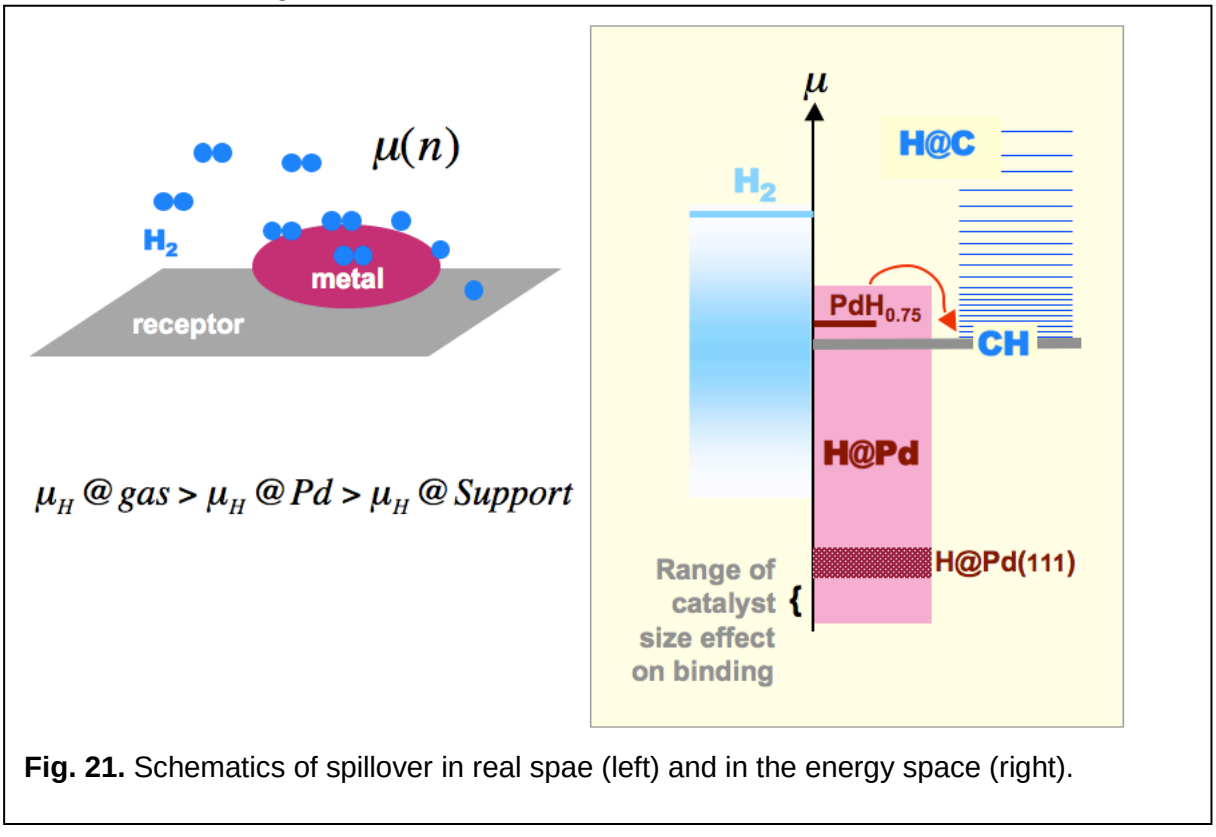

Fig. 21. Schematics of spillover in real spae (left) and in the energy space (right).

Studies of dissociative chemisorption of molecular hydrogen and desorption of atomic hydrogen on Pt clusters concluded that the number of adsorbed H_2 increases with the increasing size of the cluster. Furthermore, it showed that the binding strengths *decrease* with the increasing coverage that is, energy-states available for H raise, approximately representing the increase of the chemical potential μ_H, since the entropy contribution is less significant. At low coverage the adsorption strengths are very large and at the saturation level are closer to the energies on a fully H-covered Pt(111) surface. In contrast, the strength of an H binding to sp^2-carbon receptor is shown to *increase* with the greater coverage, due to its clustering and CH-phase formation. This analysis reconciles the fact of spillover with too weak binding of the H to the bare substrate, by stressing the role of nucleation of *condensed* CH phase which must be forming in the process of spillover on a graphene-receptor, as it is more favorable than H_2 molecule. In previous section here the catalyst *per se* was not considered, and the focus was on the variation of the hydrogen binding to the receptor and its thermodynamic comparison with gaseous H_2.

Following are important details of hydrogen binding to the catalyst particle, which serves as a gateway to the entire process and whose saturation is also an important aspect of spillover. Combining - molecular dihydrogen gas phase, H dissolved on the catalyst, and H in the “storage phase” on the receptor - all the pieces, a conceptual qualitative schematic of spillover is drawn in **Fig. 21** above. On the left, the blue line marks the energy of H in its molecular form with the additional broad (also blue) range is the chemical potential of H including the entropic contribution at different gas conditions. On the right side, a family of thin dark-blue lines corresponds to the energies of H bound to graphene, which vary with the size and the configuration of the cluster-island and converge to the CH-phase energy. The mid-section pink block shows the range of energies of H at the catalyst as computed and analyzed below. The first H_2 molecule dissociates and binds to the catalyst rather strongly, and therefore μ_H lies deep in this picture. However, the energies of the subsequent H_2 binding gradually decrease, raising the μ_H. For the spillover of an H to occur from the metal, the μ_H must exceed the CH state energy level shown by the gray line, before the metal cluster saturates (i.e., becomes unable to further accept new H_2 molecules). The catalyst plays an important role in bringing the μ_H into this range. Possible metal-hydride phase formation imposes an additional constraint on the μ_H. The former must lie above the μ_H of the receptor, to avoid formation of metal-hydride before the spillover (assuming that the hydride-phase would inhibit the catalytic activity). In this task-effort we have validated this model, by exploring through *ab initio* computations the gradual energy change of H on the catalyst, to reveal how it fits between the energy on the receptor and as free gas. Comparing these μ_H values identifies the range of chemical potential favorable for the spillover. The role of catalyst saturation and binding strength of H with the receptor in bringing the μ_H in this desirable range, was explored. Furthermore, to understand the first kinetic step, the barrier involved in the motion of an H atom from catalyst to receptor is computed and compared with the experimental observation.

In order to get the μ_H on the metal catalyst, hydrogen uptake process of a free *unsupported* cluster was performed. More specifically, we consider relatively small four-atom Ni and Pd clusters as catalysts and a graphene with the H-terminated edge as receptor. The binding energy as well as the chemical potential of H_2 on the metal cluster will depend upon the number of H_2 attached and the relative positions of the H atoms. For example, the binding energy of the first H_2 on the cluster will differ from the next H_2 and so on. Addition of a H_2 molecule leads to gain in the incremental energy, which approximately represents the chemical potential μ_H, which is defined as;

$$\mu_H = \Delta E(M_n H_m) = [E(M_n H_m) - E(H_2) - E(M_n H_{m-2})]/2,$$

where M_n is a metal-catalyst. A comparison of the $\mu_H(m)$ in the metal cluster and in the receptor provides the number of H_2 molecules required to saturate the metal cluster sufficiently to permit the spillover onto the receptor.

The geometries of Pd_4 cluster are optimized and among the various structures, a tetrahedron is found to be the lowest in energy. The magnetic moment (2 μ_B) and the Pd-Pd bond lengths (2.65 Å) in Pd_4 cluster, are in good agreement with the previous calculations performed by using the hybrid B3LYP exchange correlation functional, which gives a better description of the transition metals. The comparison provides an independent test of the method accuracy. For the subsequent hydrogenation of the catalyst, several symmetrically non-equivalent adsorption sites for a H_2 molecule on the cluster are considered and their respective energies are compared. The first H_2 dissociatively adsorbs on the Pd_4 cluster (essentially forming a hydride molecule). Among the various structures of the Pd_4H_2 there are two lowest energy configurations as was observed in the previous calculation. In one of the structures the dissociated H atoms cap the adjacent triangular faces of the Pd_4 cluster (**Figure 22** below), while in the other they bridge the Pd-Pd edges, which do not have the common Pd atom. We continued hydrogenation by subsequently adding the H_2 molecules, to the ground state structure (cluster+H_2), obtained from the previous optimization. From the 2nd H_2 onwards, H_2 molecules do not fully dissociate, but rather bind to Pd_4 via Kubas type of interaction, where the H-H bonds are elongated from 0.73 Å (as in molecular H_2) to 0.84~0.87 Å. The hydrogenation was continued until the cluster stopped to adsorb any further H_2, i.e., no bound stable configuration could be found. The Pd_4 cluster saturates after adsorbing nine H_2 molecules. The optimized geometries of these clusters are shown in **Fig. 22**. The 10th H_2 is repelled from the cluster and remains in the molecular form. This unattached H_2 lies more than 3.3 Å away from the atoms of the saturated cluster. The H-H bond length remains the same as in the molecular H_2, accompanied by almost no gain in binding energy, signaling the saturation of the cluster.

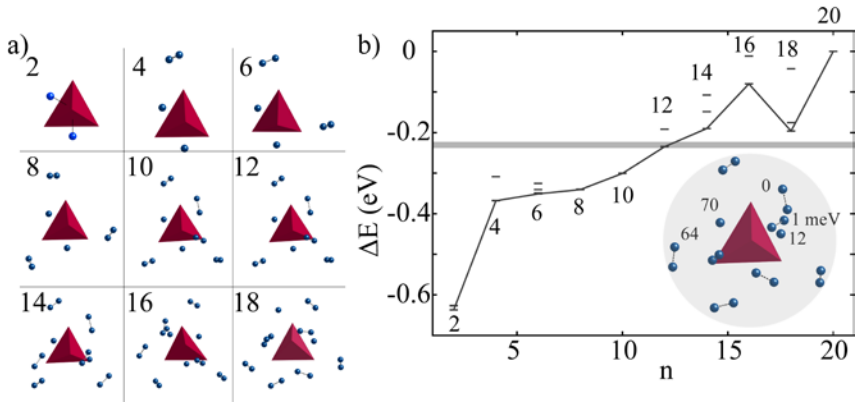

Fig. 22. Optimized structures of Pd_4H_n clusters with H atoms (left) and the corresponding energies for n = 1 -20.

The incremental energies ΔE, which are plotted, never exceed the energy of an H on a pristine graphene. Hence, thermodynamically spillover cannot be easily initiated on a pristine graphene. The possibility cannot be completely excluded, because at higher temperature due to fluctuations some of the H atoms can move to the graphene. On the other hand, the incremental binding energies do exceed the chemical potential of H in hydrogenated phase, after the adsorption of 6th H_2 molecule as shown **Fig. 22** above (the gray line there corresponds to the thin gray line in previous figure as well). Therefore, the spillover to the fully hydrogenated phase is indeed thermodynamically favorable after the catalyst has adsorbed six H_2 molecules.

Due to computational limitations, we used a small cluster to model the catalyst, but the qualitative conclusions on spillover are quite general. Although we believe that the overall chemisorption behavior of catalyst does not change much with increasing size, some additional complications may appear. Among them could be possible bulk metal-hydride phase formation. In order to assess this, we have separately calculated chemical potential of H in the Pd-hydride crystal ($PdH_{0.75}$) using standard periodic boundary conditions instead of cluster approach. The result is shown by the dark red line, which lies ~60 meV above the gray CH-line. Hence, in the case of Pd the spillover will occur before formation of hydride. The position of this line may vary for different metal catalysts, which is helpful in determining the best metal catalyst for spillover, and could be further tuned/optimized by alloying. We also calculate the adsorption energy of the H on Pd(111) surface, for coverage from 0.25 ML to 1 ML, shown by red block. The adsorption energy of 0.25 ML hydrogen is 0.57 eV, only slightly higher (~0.1 eV) than that in the Pd_4. Hence, with increasing cluster size the threshold of the spillover may decrease but not very significantly.

Additionally, in order to study the effect of different metal element catalysts on the spillover, we also carried out simulated hydrogenation of a Ni_4 cluster. The ground state geometry of the Ni_4 is found to be a tetrahedron, with the Ni-Ni bond length of 2.60 Å and magnetic moment of 4 μ_B. The larger magnetic moment arises due to localized nature of the Ni *3d* orbital. The Ni_4 adsorbs the first two H_2 molecules dissociatively. The cluster saturates after adsorbing the 10th H_2 molecule. The incremental binding energy exceeds the chemical potential of H in hydrogenated

phase, after the adsorption of the 7th H_2. Therefore, the effect of changing the metal from Pd to Ni essentially shifts the threshold of the spillover from 6th to 7th H_2, because of the more diffused nature of Pd *4d* orbital compared with the Ni *3d* orbital. The overall trend in the hydrogenation of the Ni_4 cluster remains similar to the Pd_4, therefore, further analysis is carried out only on the Pd_4 cluster.

The justification of considering incremental energies as chemical potential (essentially an average quantity), depends on how large the variance is in the removal energies of the different H atoms, from a saturated cluster/catalyst. The energy cost to remove an H from the cluster may in principle differ with the type/position of the removed atom. In order to evaluate this, we have calculated the removal energies of the 5-symmetrically non-equivalent H-atoms including Kubas and dissociated from fully saturated Pd_4H_{18} as shown in **Fig. 22b**, inset. The difference in removal energies of the five non-equivalent atoms lies within 70 meV, which is relatively small. This energy difference is within 15 % of the total range of chemical potential of H on a catalyst, and is reasonable enough to justify its use as a chemical potential. This difference is expected to decrease with the increasing size of the catalyst. Moreover, the bonding strengths of the Kubas type H atoms are similar to the dissociatively adsorbed H atoms, indicating that any atom could potentially participate in the spillover process, as long as μ_H of the system has reached high enough level at overall saturation.

The above analysis has demonstrated that it is energetically possible for spillover to occur from an unsupported metal cluster to a receptor. In experiments these clusters are supported on the substrate, and hydrogen diffuses (or rather hops) from the catalyst to the support/receptor. In order to make our model closer to the experimental situation, we next studied the hydrogenation of a *supported* cluster on a receptor. The pristine graphene was chosen as support as the C atoms in the vicinity of the catalyst might exhibit improved binding with the hydrogen. First, several non-equivalent sites for Pd_4 cluster on graphene have been optimized. After relaxation, however, most of the configurations converge to a structure, where three corners of the tetrahedron lie above the centers of C-C bond, **Fig. 23**. There are two types of Pd-Pd bond with the bond lengths of 2.60 and 2.69 Å, respectively, whereas average Pd-C bond lengths are 2.30 Å. The binding energy and the total magnetic moment of the whole Pd_4 cluster on the graphene are 0.42 eV and 1 μ_B (reduced from the unsupported cluster), respectively.

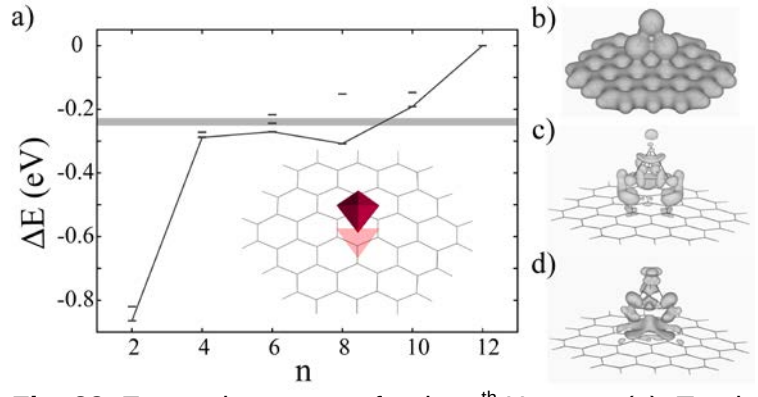

Fig. 23. Energy increments for the nth H-atoms (a). Total (b), accumulation (c), and depletion (d) charges.

The bonding of receptor and catalyst is analyzed by plotting the total, accumulation, and depletion of charges, as shown in **Fig. 23 b-d**. The accumulation/depletion of charges is obtained by subtracting the total charges of free Pd_4 cluster and graphene calculated independently, with the

same atomic position, from the total charge of the Pd_4@graphene. The positive (negative) value of the isosurface represents the accumulated (depleted) charge regions. The total charge density shows some directionality of the C-Pd bond, nevertheless, the charges around Pd are diffused, a signature of a mixed covalent and metallic bonding (b). Further evidence comes from the isosurfaces of accumulation and depletion, as the charge has been accumulated between the C-Pd bonds and depleted from the π-cloud of hexagonal ring in graphene, c and d.

Next, the hydrogenation of this supported cluster was performed, following the same procedure as described above for the free cluster. Like the free cluster, the first H_2 is adsorbed dissociatively and subsequent ones bind via Kubas interaction. The cluster saturates with five H_2 molecules, much sooner than the free cluster. As expected, the incremental adsorption energy never exceeds the energy of an H on pristine graphene. However, it does cross the level-line of C-H energy of a fully hydrogenated graphene after the adsorption of the 5^{th} H_2 molecule, hence showing the thermodynamic possibility of the spillover. The onset of spillover occurs earlier than in the free cluster because the charge available for binding with the H_2 is now shared with the support material. This reduces the overall intake of H on the catalyst, with no harm to spillover.

Having shown the possibility of the spillover from both free and supported cluster, we turned to the kinetics aspects, which essentially involve the motion of the H atom from the metal to the receptor. The likelihood of an H atom to hop from the catalyst to the pristine graphene substrate was tested in a computational experiment, by removing the H atom from the saturated catalyst and bringing it to the receptor. Upon relaxation, H goes back to the catalyst spontaneously. When the removed hydrogen is placed farther away from the catalyst, it remains attached but the whole process is endothermic by 2.5 eV, highlighting again the difficulty of spillover on pristine graphene. Similarly, we tested an H atom hopping to the receptor in the vicinity of a fully hydrogenated graphene phase, which was represented by hydrogenated ring-hexagon near the catalyst. In this case, the H-atom removed from the catalyst is more stable on the hydrogenated phase: unlike in pristine graphene case, the H does not come back to the catalyst, and the overall process becomes energetically favorable by 0.15 eV, making spillover possible on hydrogenated graphene.

In summary of this task-effort, we have shown the thermodynamic and kinetic plausibility of the spillover process. Energetically it is possible for spillover of H to occur from a metal cluster to the hydrogenated graphene, both from the freestanding and from the receptor supported clusters. Importantly, the process does not require full saturation of the cluster because thermodynamically spillover becomes favorable even before a cluster saturates. Furthermore, it is energetically unfavorable for the spillover to occur on a pristine graphene surfaces, yet a phase of hydrogenated graphene facilitates the process by significantly improving the C-H binding. The migration barrier for hydrogen from the metal cluster to the hydrogenated phase is small, suggesting that the spillover can easily occur below room temperature. These findings are in agreement with the recent experiments, where H-uptake via the spillover increases with the temperature and the reduction of the substrate. Moreover this work provides possibly the first explanation of the “nano-

thermodynamics" of spillover and also hints towards finding materials where it can be achieved more effectively. Along with the catalyst saturation, the optimum C-H bonding has emerged as an important factor for the spillover. Therefore any modification of the receptor that leads to an increase in this energy will also enhance the spillover (of course, within the reversibility limits). The incorporation of defects, curvature, and dopants are a few of the potential routes to facilitate nucleation by improving the C-H binding. For example, this has been demonstrated for graphene where the energy of hydrogenation changes drastically by Stone-Wales type of defects.

A few words must be said about the computational methods used in this catalyst-function study. The calculations are based on the density-functional method with all-electron projected augmented wave potentials and the generalized gradient approximation of the Perdew–Burke–Ernzerhof (PBE) for exchange and correlation, as implemented in VASP. Gamma point is used for Brillouin zone sampling. Conjugate gradient scheme is employed to relax the geometry until the forces on every atom are less than 0.005 eV/Å. Large vacuum spaces (~15 Å) are used in supercells to minimize any cell-cell spurious interactions. The migration barrier for an H-atom is calculated using nudged elastic band method.

Di-hydrogen binding in metallacarboranes

We have explored the possibilities of using transition metal atoms in metallacarboranes, as a linker to the carboranes and additionally to bind di-hydrogen ligands via Kubas type of interaction, **Fig. 24**. We studied the H_2 adsorption on Ti based metallacarborane $Ti_2(C_2B_8H_{10})$. It can adsorb upto 9 H_2 molecules, which is equivalent to the 7.7 wt%. There are 2 carbon atoms available for the linkers to form the MOFs. The binding energies of hydrogen lie within the 0.14-0.26 eV, which are ideal for the reversible adsorption. We choose the smallest metallacarborane cluster for this study. We find that the Sc and Ti can sorb maximum number of H_2 molecule. The uptake decreases with the increasing number of d electrons. Furthermore the so-called 18 e rule is violated in metallacarboranes and may need further scrutiny.

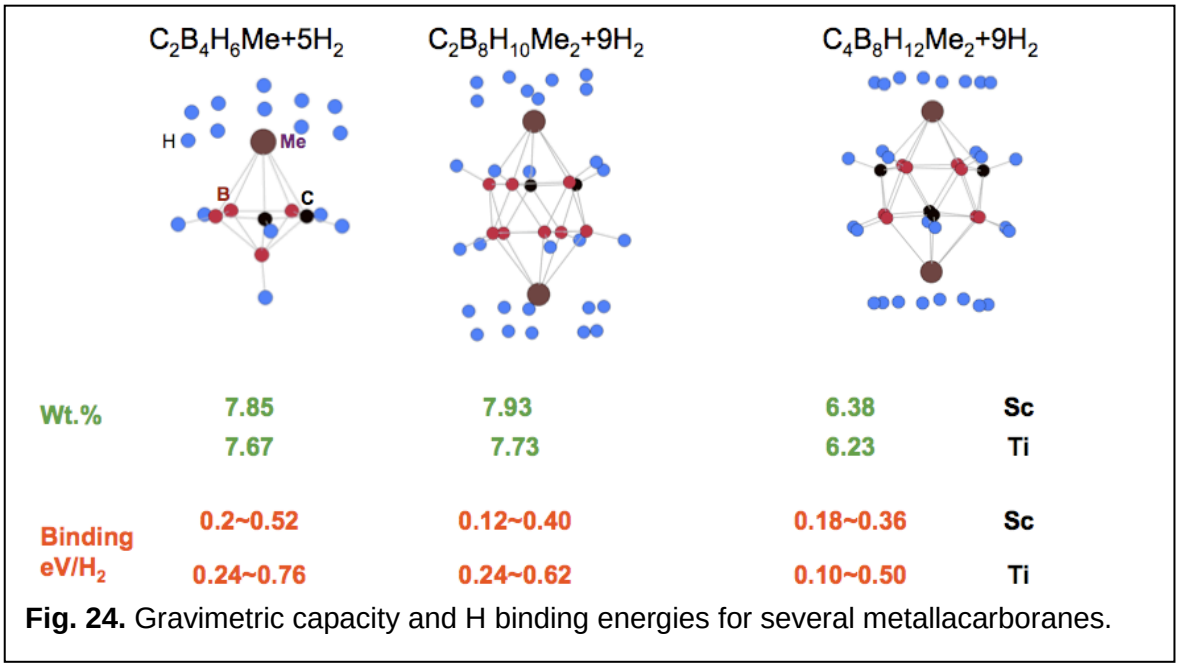

Fig. 24. Gravimetric capacity and H binding energies for several metallacarboranes.

We also performed studies on larger cluster $C_4B_8H_{12}Me_2$. Upon hydrogenation this cluster stores upto 9 H_2 molecules, which corresponds to 6.38 wt%. Therefore, the storage in the metallacarboranes peaks for icosahedral $C_2B_8H_{10}Me_2$ cluster. Furthermore the experimentally observed MOF have icosahedral carboranes as a linker which are corresponding counterpart of this metallacarborane. Actual storage in metallacarborane based MOF's will be sum of Kubas and physisorbed H_2 molecules, **Fig. 25**. Therefore, the metallacarborane based MOFs are indeed a promising material for hydrogen storage and can meet the DOE 2015 goals.

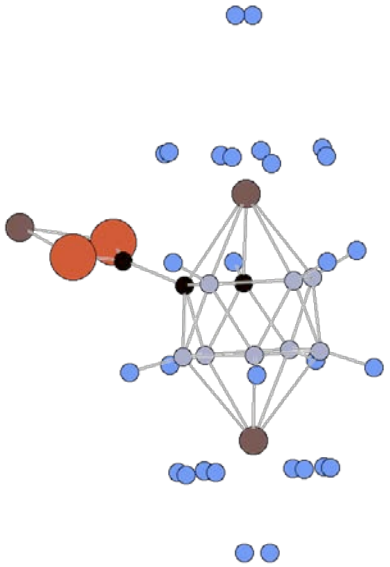

Fig. 25. Metallacarborane cluster shows Kubas-bonded H_2 molecules and, additionally, more remote physisorbed H_2 as well.

Conclusions

Although each or the tasks and topics described above has its own end-results and conclusions, it is important and helpful to add an overall summary of general, higher-level conclusions highlighting the main findings and perhaps suggesting what work must be considered as worthwhile investment in the future.

- Our analysis shows, along with the negative outcome of repeated experimental tests, that storage of hydrogen on *pure carbon nanotube* systems is not feasible.
- On the other hand, the light weight of carbon and the utmost high surface area of its *sp^2-forms make it very attractive* storage media.
- Option one is physisorption on highly porous *3D-foamlike architectures*. Optimal size of pores of ~0.7-1 nm invokes the H_2 interaction in "all-6" directions (simplistically, for a cube-cavity) and thus the achieved superposition of weak van der Waals bindings can create an overall sufficiently deep potential well.
- This physisorption can further be enhanced by *doping of C-networks*, notably doping by another light element boron, CB_x. This deserves further investigation.
- Another distinctly different path is *chemisorption on carbon substrates*, with one particular mechanism known as *spillover*. Spillover remains a controversial mechanism, yet our analysis of its thermodynamics and kinetics suggest important potential for further research, with promise of reaching operating requirements.
- One useful parallel which we have explored soon after completion of this project is between the *H storage and the Li storage* on sp^2-carbon electrodes: in both cases the issues of thermodynamics and kinetics within the charge/discharge cycles are of paramount importance. We believe that additional value knowledge may be uncovered from *concurrent research of both topics*. Certainly, in theoretical/computational investigation, where the methods can be similar, such study is bound to bring a great deal of synergy, and deserves the DOE attention.

Publications

1. H. Cheng, and B.I. Yakobson, “Designing carbon nanoframeworks tailored for hydrogen storage”, P.F. Weck, E. Kim, N. Balakrishnan, ***Chem. Phys. Lett.***, **439**, 354 (2007).
2. F. Ding, Y. Lin, P. Krasnov, and B.I. Yakobson, “Nanotube derived carbon foam for hydrogen storage”, ***J. Chem. Phys.***, **127**, 164703 (2007).
3. P.O. Krasnov, F. Ding, A.K. Singh, and B.I. Yakobson, “Clustering of Sc on SWNT and reduction of hydrogen uptake: ab initio all-electron calculations”, ***J. Phys. Chem. C, Letters***, **111**, 17977 (2007).
4. “Hydrogen storage by spillover on graphene as a phase nucleation process”, Y. Lin, F. Ding, and B.I. Yakobson, ***Phys. Rev. B***, **78**, 041402(R) (2008).
5. O.V. Pupysheva, A.A. Farajian, and B.I. Yakobson, “Fullerene nanocage capacity for hydrogen storage”, ***Nano Letters***, **8**, 767 (2008).
6. A.K. Singh, M. A. Ribas, and B.I. Yakobson, “H-Spillover through the Catalyst Saturation: An Ab Initio Thermodynamics Study”, ***ACS Nano***, **3**, 1657 (2009).
7. “Hydrogen storage capacity of carbon-foams: Grand canonical Monte Carlo simulations”, A.K. Singh, J. Lu, R.S. Aga, and B.I. Yakobson, ***J. Chem. Phys. C***, **115***,* 2476–2482 (2011).
8. “Calcium-decorated carbyne networks as hydrogen storage media”, P.B. Sorokin, H.K. Lee, L.Yu. Antipina, A.K. Singh, and B.I. Yakobson, ***Nano Lett.***, **11**, 2660–2665 (2011).
9. “Challenges in hydrogen adsorptions: from physisorption to chemisorptions”, F. Ding and B.I. Yakobson, ***Frontiers of Physiscs,*** **6**, 142-150 (2011).
10. “Metallacarboranes: Towards promising hydrogen storage metal-organic frameworks”, A.K. Singh, A. Sadrzadeh, and B.I. Yakobson, ***J. Amer. Chem. Soc.***, **132**, 14126–14129 (2010).
11. “Metal-assisted hydrogen storage on Pt-decorated single-walled carbon nanohorns”, Y. Liu, C.M. Brown, D.A. Neumann, D.B. Geohegan, A.A. Puretzky, C.M. Rouleau, H. Hu, D. Styers-Barnett, P.O. Krasnov, B.I. Yakobson, ***Carbon***, **50**, 4953–4964 (2012).
12. “First principles calculations of H-storage in sorption materials”, A.K. Singh and B.I. Yakobson, ***J. Mater. Science***, **47**, 7356-7366 (2012).
13. “Unfolding the fullerene: Nanotubes, graphene and poly-elemental layers” E.S. Penev, V.I. Artyukhov, F. Ding and B.I. Yakobson, ***Advanced Materials***, **24**, 4956 (2012).